

# Nonlinear transmission spectroscopy with dual frequency combs

Rachel Glenn and Shaul Mukamel

*Department of Chemistry, University of California, Irvine, California 92697-2025, USA*

(Dated: March 2, 2022)

## Abstract

We show how two frequency combs  $\mathcal{E}_1$ ,  $\mathcal{E}_2$  can be used to measure single-photon, two-photon absorption (TPA), and Raman resonances in a molecule with three electronic bands, by detecting the radiofrequency modulation of the nonlinear transmission signal. Some peaks are shifted by the center frequency of the comb and have a width close to the comb width. Other peaks are independent of the carrier frequency of the comb. TPA and Raman resonances that are independent of the carrier frequency are selected by measuring the transmission signal  $\sim \mathcal{E}_1^2 \mathcal{E}_2^2$  and the single-photon resonances are selected by measuring the transmission signal  $\sim \mathcal{E}_1^3 \mathcal{E}_2$ . that interacts three times with comb 1. Sinusoidal spectral phase shaping strongly affects the TPA resonances, but not the Raman resonances, for an even or odd phase profile around a selected resonance.

PACS numbers: 42.65.Re, 42.65.Re, 41.85.Ct

## I. INTRODUCTION

Optical frequency combs, first introduced in 1999[1], have revolutionized metrology[1, 2] due to their high resolution of optical frequencies. They have been employed for calibrating sources of spectrographs in astronomy[3], identifying multiple molecules simultaneously[4], Doppler-free spectroscopy[5–7], improving energy efficiency in environmental monitoring[8], and forensic analysis, among its many applications. This technology has also enabled the generation of attosecond pulses[9]. Because the measurement times of the interferometric signal can be shortened from seconds using conventional pulse techniques, such as the scanning-arm Michelson interferometer[10], to microseconds with dual-comb; future possible applications include the observation of chemical reactions in real time[11].

Dual comb Fourier transform spectroscopy [8, 12–17] is a technique employed for its spectral resolution and its concise recording times compared to conventional Fourier transform spectroscopy[18]. It employs two coherent broadband optical frequency combs and records the nonlinear transmission in the time domain. A Fourier transformation reveals Raman resonances in the radio-frequency regime[13, 15, 18–24]. Previously, the spectrum was calculated numerically by means of calculating the intensity of light transmitted through an absorbing gas[21] or by means of fitting with the nonlinear least-squares method[19]. Here we calculate the third order signal obtained with two frequency combs and connect them to the third order susceptibility  $\chi^{(3)}$ . We address several issues: how the peaks map from the optical to the radio-frequency regime; how do the single-photon and two-photon resonances show up in the transmission spectrum; how to selectively detect the TPA, Raman, and single-photon resonances in the transmission spectrum; and can we control these resonances by means of pulse shaping. We find the positions of some peaks are sensitive to the carrier frequency of the frequency comb, while other peaks not sensitive to carrier frequency. New peaks not studied previously[13, 15, 18–24] are calculated.

Pulse-shaping allow the control of the phase  $\phi(\omega)$  and amplitude  $\tilde{\mathcal{E}}(\omega)$  of the electric field  $\mathcal{E}(\omega)$

$$\mathcal{E}(\omega) = \tilde{\mathcal{E}}(\omega)e^{i\phi(\omega)} \quad (1)$$

and has inspired the generation of arbitrary waveforms at optical frequencies [25–28]. We investigate how a sinusoidal phase added to the frequency comb affects the peaks in the spectrum.

This paper is organized as follows. In Sec. II we write the expressions for the nonlinear transmission spectrum. The transmission signal with of a Lorentzian pulse is plotted in Sec. III.

The frequency comb in the time and frequency domain is presented in Sec. IV. The selection of the comb line numbers in the transmission spectrum and simulation of the transmission spectrum is given in Sections V and VI. The comb transmission for a sinusoidal spectral phase is simulated in Sec. VII. The summary is presented in Sec. VIII.

## II. THE NONLINEAR TRANSMISSION SIGNAL

We calculate the transmission signal measured in the time domain and Fourier transformed to give the transmission spectrum[32]

$$S_t(\omega_s) = -\frac{2}{\hbar} \mathcal{I} \int dt e^{i\omega_s t} \mathcal{E}^*(t) P(t), \quad (2)$$

this yields

$$S_t(\omega_s) = -\frac{2}{\hbar} \mathcal{I} \int d\omega' \tilde{\mathcal{E}}^*(\omega' - \omega_s) P(\omega'), \quad (3)$$

where  $P(\omega)$  is the polarization induced in the matter by the light and  $\mathcal{I}A(\omega)$  denotes the imaginary part. The polarization will be expanded in powers of the radiation field[32]

$$P(\omega) = P^{(1)}(\omega) + P^{(3)}(\omega). \quad (4)$$

The first-order polarization is given by

$$P^{(1)}(\omega) = \mathcal{E}(\omega) \chi^{(1)}(\omega), \quad (5)$$

where  $\chi^{(1)}(\omega)$  is the linear susceptibility. Inserting  $P^{(1)}(\omega)$  into Eq. (3) gives

$$S_t^{(1)}(\omega_s) = -\frac{2}{\hbar} \mathcal{I} \int d\omega' \tilde{\mathcal{E}}^*(\omega' - \omega_s) \mathcal{E}(\omega') \chi^{(1)}(\omega'). \quad (6)$$

The third order polarization is given as[32]

$$\begin{aligned} P^{(3)}(\omega) = & \int d\omega_1 d\omega_2 d\omega_3 \mathcal{E}(\omega_1) \mathcal{E}(\omega_2) \mathcal{E}^*(\omega_3) \\ & \times \chi^{(3)}(-\omega; \omega_1, \omega_2, \omega_3) 2\pi \delta(\omega - \omega_1 - \omega_2 + \omega_3), \end{aligned} \quad (7)$$

where the susceptibility will depend upon the model of the system. Inserting Eq. (7) into Eq. (3) gives

$$\begin{aligned} S_t^{(3)}(\omega_s) = & -\frac{2}{\hbar} \mathcal{I} \int d\omega' d\omega_1 d\omega_2 d\omega_3 \tilde{\mathcal{E}}^*(\omega' - \omega_s) \tilde{\mathcal{E}}(\omega_2) \tilde{\mathcal{E}}^*(\omega_3) \\ & \times \tilde{\mathcal{E}}(\omega_1) 2\pi \delta(\omega' - \omega_1 - \omega_2 + \omega_3) \chi^{(3)}(-\omega', \omega_1, \omega_2, \omega_3). \end{aligned} \quad (8)$$

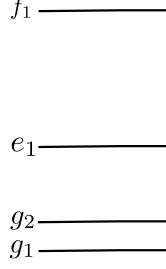


FIG. 1: The model level scheme contains three electronic states with the transition frequencies

$\omega_{f_1g_1} = 36,000\text{cm}^{-1}$ ,  $\omega_{e_1g_1} = 12,000\text{cm}^{-1}$ ,  $\omega_{g_2g_1} = 1,200\text{cm}^{-1}$ . The dephasing rates are  $\Gamma_{f_1g_1} = 500\text{cm}^{-1}$ ,  $\Gamma_{e_1g_1} = 100\text{cm}^{-1}$ ,  $\Gamma_{g_2g_1} = 80\text{cm}^{-1}$ . The transition dipole moments are set to one.

Equation (8) will be used to calculate the transmission spectrum with a single broadband pulse and with a shaped-pulse composed of two frequency combs.

For comparison we also examine the heterodyne detected signal, i.e., transmission spectrum, measured in the frequency domain, called the frequency-dispersed transmission spectrum[32]

$$\mathcal{S}_f(\omega) = -\frac{2}{\hbar}\mathcal{I}\tilde{\mathcal{E}}^*(\omega)P(\omega). \quad (9)$$

Inserting Eq. (5), the first-order signal is given as

$$\mathcal{S}_f^{(1)}(\omega) = -\frac{2}{\hbar}\mathcal{I}|\tilde{\mathcal{E}}(\omega)|^2\chi^{(1)}(\omega). \quad (10)$$

Unlike Eq. (6), the signal does not depend upon the phase of the field.

Using Eq. (7), the third order dispersed spectrum is given as

$$\begin{aligned} \mathcal{S}_f^{(3)}(\omega) = & \mathcal{I}\frac{2}{\hbar}\mathcal{E}^*(\omega) \int d\omega_1 d\omega_2 d\omega_3 \mathcal{E}(\omega_1)\mathcal{E}(\omega_2)\mathcal{E}^*(\omega_3) \\ & \times \chi^{(3)}(-\omega; \omega_1, \omega_2, \omega_3) 2\pi\delta(\omega - \omega_1 - \omega_2 + \omega_3). \end{aligned} \quad (11)$$

In the next section, we compare Eqs. (8) and (11) for a single pulse.

### III. TRANSMISSION SIGNAL OF A BROADBAND PULSE

We consider a three band model system Fig. 1 with electronic states  $|g\rangle$ ,  $|e\rangle$ ,  $|f\rangle$ . The linear susceptibility then reads[32]

$$\chi^{(1)}(\omega) = \sum_{e_1g_1} -\frac{1}{\hbar}|\mu_{e_1g_1}|^2 G_{e_1g_1}(\omega), \quad (12)$$

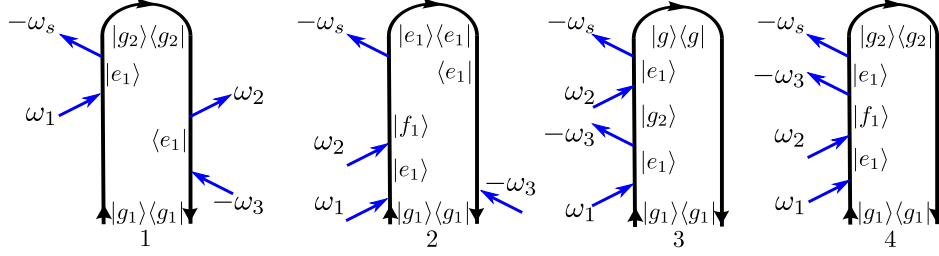


FIG. 2: (Color online) Loop diagrams for the transmitted signal Eq. (8) or Eq. (11).

where  $G_{e_1g_1}(\omega) = (\omega - \omega_{e_1g_1} + i\Gamma_{e_1g_1})^{-1}$ .

The third-order susceptibility can be read off the diagrams of Fig. 2 [32]

$$\begin{aligned}
\chi^{(3)}(-\omega; \omega_1, \omega_2, \omega_3) &= \left(\frac{-1}{2\pi\hbar}\right)^3 \sum_{g_i, e_i, f_i} V_{g_1e_1} V_{e_1g_2} V_{g_2e_1} V_{e_1g_1} \\
&\times G_{e_1}^*(-\omega + \omega_1 + \omega_2) G_{g_2}^*(-\omega + \omega_1) G_{e_1}(\omega_1) + V_{g_1e_1} V_{e_1f_1} \\
&\times V_{f_1e_1} V_{e_1g_1} G_{e_1}^*(-\omega + \omega_1 + \omega_2) G_{f_1}(\omega_1 + \omega_2) G_{e_1}(\omega_1) \\
&+ V_{g_1e_1} V_{e_1g_2} V_{g_2e_1} V_{e_1g_1} G_{g_2}(\omega_1 - \omega_3) G_{e_1}(\omega_1 - \omega_3 + \omega_2) \\
&\times G_{e_1}(\omega_1) + V_{g_1e_1} V_{e_1f_1} V_{f_1e_1} V_{e_1g_1} G_{e_1}(\omega_1 + \omega_2 - \omega_3) \\
&\times G_{f_1}(\omega_1 + \omega_2) G_{e_1}(\omega_1).
\end{aligned} \tag{13}$$

The frequency-dispersed transmission spectrum Eq. (11) with a Lorentzian pulse[33]

$$\mathcal{E}(\omega) = \frac{\sigma}{\omega + i\sigma} \tag{14}$$

is calculated analytically and shown in the top row of Fig. 3.  $\mathcal{S}_f^{(3)}(\omega_s)$  is plotted in the units  $\frac{2\pi}{\hbar} \left(\frac{1}{2\pi 10,000\hbar}\right)^3$  with the dipole moments set to one. In Fig. 3(a), the resonances  $\omega = \omega_{f_1e_1}, \omega_{e_1g_1}, \omega_{e_1g_2}$  are marked. The transmission spectrum contains other peaks such as  $\omega_s = \omega_c - \omega_{g_2g_1}, \omega_{f_1g_1} - \omega_c$ . The  $\omega_s = \omega_{f_1g_1} - \omega_c$  peak overlaps with the  $\omega_s = \omega_{e_1g_1}$  peak. The dominate peak in the transmission spectra is the peak at the carrier frequency  $\omega_s = \omega_c$ . As the pulse width increases, in Fig. 3(b), the  $\omega_s = \omega_{f_1g_1}, \omega_{e_1g_2}$  peaks become seen and the  $\omega_c$  peak decreases. Increasing the pulse width further, Fig. 3(c), these peaks become more pronounced.

The Fourier transform of the time-resolved transmission signal Eq. (8) is shown the bottom row of Fig. 3 for the electric field (14). In Fig.3(a), the two-photon transition  $\omega_{f_1g_1}$  interacts two times with the pulse and it is shifted by  $2\omega_c$ . The single-photon transitions,  $\omega_{e_1g_1}, \omega_{f_1e_1}$ , interact once with pulse and are shifted by  $\omega_c$ . The Raman peaks are not shifted, since they interact twice

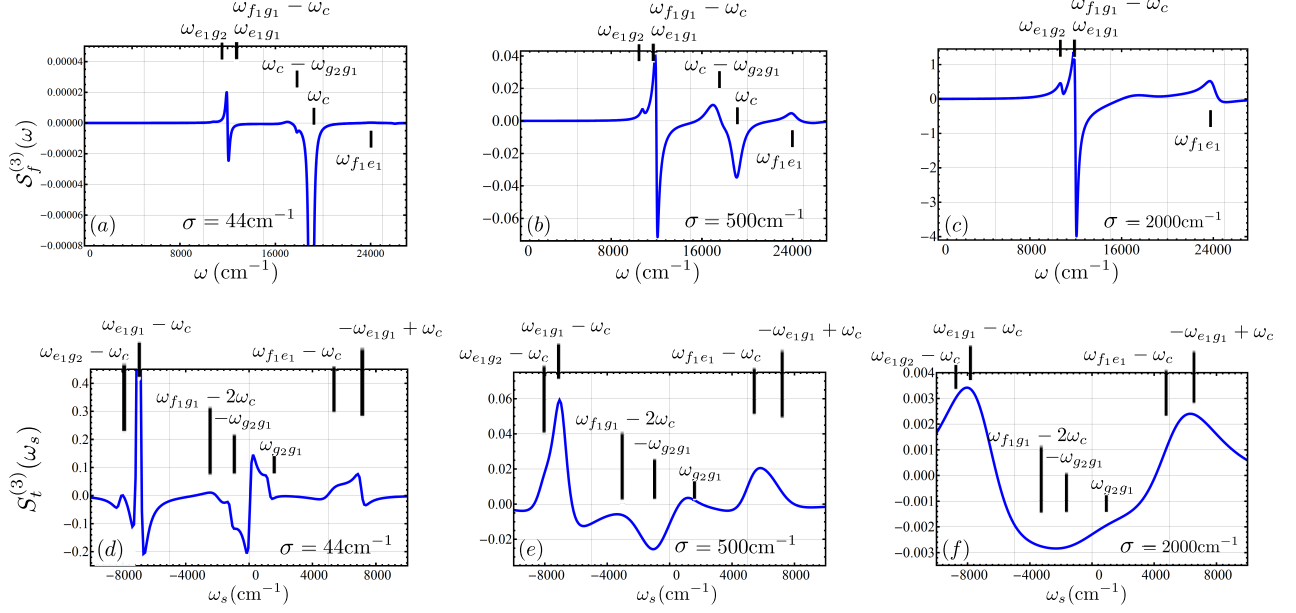


FIG. 3: (Color online) Top: The frequency-dispersed transmission spectrum  $\mathcal{S}_f^{(3)}(\omega)$  Eq. (11) is plotted for a Lorentzian pulse Eq. (14), for several values of  $\sigma$ . Bottom: The Fourier transform of the time-resolved transmission signal  $\mathcal{S}_t^{(3)}(\omega_s)$  Eq. (8) is plotted for a Lorentzian pulse Eq. (14), for several values of  $\sigma$ . The signal is plotted in the units  $\frac{2\pi}{h}(\frac{1}{2\pi 10,000\hbar})^3$  and the carrier frequency is  $\omega_c = 19000 \text{ cm}^{-1}$ . All dipole moments are set to one.

with the pulse, once with  $\omega_c$  and a second with  $-\omega_c$ , which cancels. Increasing the pulse width to  $\sigma = 500 \text{ cm}^{-1}$  in Fig. 3(e) the  $\omega_s = \omega_{e_1 g_1} - \omega_c$  peak remains dominate. This is also true for Fig. 3(b). Increasing the pulse width further, in Fig. 3(f) The peaks become smeared. Overall, the two signals  $\mathcal{S}_f^{(3)}(\omega)$  and  $\mathcal{S}_t^{(3)}(\omega_s)$  are different.

#### IV. THE DUAL FREQUENCY COMB

The frequency comb is generated using a mode-locked laser that produces a series of optical pulses separated by the round-trip time of the laser cavity  $T_{rep} = l_c/v_g$ , where  $v_g$  is the group velocity and  $l_c$  is the round-trip length of the laser cavity[12, 34–36]. We consider two femtosecond

frequency combs, which with the electric field  $E(t) = \mathcal{E}(t) + \mathcal{E}^*(t)$

$$\begin{aligned} \mathcal{E}(t) = & e^{-i\omega_c t} \sum_{n=1}^N \tilde{\mathcal{E}}(t + nT_{rep,1}) e^{in(\omega_{ceo,1} + \omega_c)T_{rep,1}} \\ & + e^{-i\omega_c(t-\Delta t)} \sum_{n=1}^N \tilde{\mathcal{E}}(t + nT_{rep,2} - \Delta t) e^{in(\omega_{ceo,2} + \omega_c)T_{rep,2}}, \end{aligned} \quad (15)$$

where  $\omega_c$  is the carrier frequency and  $\Delta t$  is the delay between the two combs. The summation index  $n$  represents the pulse number with a total of  $N$  pulses. The envelope function  $\tilde{\mathcal{E}}(t)$  is periodic  $\tilde{\mathcal{E}}(t) = \tilde{\mathcal{E}}(t + nT_{rep})$ . The repetition frequencies  $\omega_{rep,1} = 2\pi/T_{rep,1}$  and  $\omega_{rep,2} = 2\pi/T_{rep,2}$  are close, such that  $\delta\omega_{rep} \ll \omega_{rep,1}$ , where  $\delta\omega_{rep} = \omega_{rep,1} - \omega_{rep,2}$ .

$\omega_{ceo,i} = (\Delta\phi/2\pi)\omega_{rep,i}$  is the carrier-envelope offset frequency.  $\Delta\phi = (1/v_g - 1/v_p)l_c\omega_c$ , is the phase shift between the peak of the envelope and the closest peak of the carrier wave and  $v_p$  is the phase velocity. The range of the carrier-envelope phase is  $0 < \Delta\phi < 2\pi$ . It is possible to lock  $\omega_{ceo,i}$  to zero[35]. We assume a vanishing carrier-offset frequency  $\omega_{ceo,1} = \omega_{ceo,2} = 0$ .

The frequency comb can be generated by replacing the cavity with a Fabry-Pérot etalon, [37]. In this method the individual pulse-shape in the pulse train becomes asymmetric. An intracavity etalon is typically employed for self-stabilization of the optical frequencies and the pulse repetition rate in conventional frequency comb generation with high repetition rates 10 GHz[38]. An external molecular absorption cell can also be employed to stabilize the optical frequencies and the optical repetition rate[39].

An ideal frequency comb uses an infinite train of pulses ( $N \rightarrow \infty$ ) and the electric field can be represented as a Fourier series,

$$\begin{aligned} \mathcal{E}(t) = & \mathcal{E}_1(t) + \mathcal{E}_2(t - \Delta t) \\ = & e^{-i\omega_c t} \sum_{n=-\infty}^{\infty} A_{n,1} e^{-in\omega_{rep,1}t} \\ & + e^{-i\omega_c(t-\Delta t)} \sum_{m=-\infty}^{\infty} A_{m,2} e^{-im\omega_{rep,2}(t-\Delta t)}, \end{aligned} \quad (16)$$

where  $A_{n,i}$

$$A_{n,i} = \frac{1}{T_{rep,i}} \int_{-\infty}^{\infty} \mathcal{E}_i(t) e^{-i(n\omega_{rep,i} - \omega_c)t} dt, \quad (17)$$

$\mathcal{E}_i(t)$  is the pulse envelope, the index  $i$  represents comb 1 or comb 2.

The Fourier transform  $\mathcal{E}(\omega) = \int_{-\infty}^{\infty} \tilde{\mathcal{E}}(t)e^{i\omega t}dt$  of Eq. (15) produces a frequency comb

$$\begin{aligned} \mathcal{E}(\omega) = & \tilde{\mathcal{E}}(\omega - \omega_c) \sum_n^N e^{in\omega T_{rep,1} + in\Delta\phi} \\ & + \tilde{\mathcal{E}}(\omega - \omega_c) \sum_m^N e^{im\omega T_{rep,2} + im\Delta\phi - i\omega\Delta t} \end{aligned} \quad (18)$$

with comb envelope  $\tilde{\mathcal{E}}(\omega) = \int_{-\infty}^{\infty} \tilde{\mathcal{E}}(t)e^{-i\omega t}dt$ . The summation of the exponentials in Eq. (18) is Fourier series with constructive interference occurring at  $\omega T_{rep,i} - \Delta\phi = 2\pi n$ . The center frequency of line number  $n$ , with  $\omega \rightarrow \omega_n$  is expressed as  $\omega_n = n\omega_{rep,i} + \omega_{ceo,i}$ . As the number of pulses  $N$  is increased the spectral width of the comb lines narrows and for  $N \rightarrow \infty$  Eq. (18) can be simplified as

$$\begin{aligned} \mathcal{E}(\omega) = & \omega_{rep,1} \tilde{\mathcal{E}}_1(\omega - \omega_c) \sum_{n=-\infty}^{\infty} \delta(n\omega_{rep,1} - \omega) \\ & + \omega_{rep,2} \tilde{\mathcal{E}}_2(\omega - \omega_c) e^{-i\omega\Delta t} \sum_{m=-\infty}^{\infty} \delta(m\omega_{rep,2} - \omega). \end{aligned} \quad (19)$$

Equation (19) is plotted in Fig. 4 for a Gaussian envelope

$$\begin{aligned} \tilde{\mathcal{E}}_1(\omega - \omega_c) &= E_1 e^{-(\omega - \omega_c)^2 / 2\sigma^2}, \\ \tilde{\mathcal{E}}_2(\omega - \omega_c) &= E_2 e^{-(\omega - \omega_c)^2 / 2\sigma^2}, \end{aligned} \quad (20)$$

with  $\sigma = 441\text{cm}^{-1}$ ,  $\omega_c = 12580\text{cm}^{-1}$  and the delta-function is replaced by a Lorentzian function. Fig. 4(a) shows the Gaussian envelope of the two overlapping frequency combs. There are 315, 416 pulses contained in the full width half max (FWHM). Fig. 4(b) shows the equidistant comb lines of the two frequency combs, in blue and red, for  $\omega_{rep,1} = 0.033\text{cm}^{-1}$  and  $\delta\omega_{rep} = 10^{-6}\omega_{rep,1}$ .

The beating of the two combs Eq. (16) creates a time resolved interferometric signal  $I(t) = |\mathcal{E}(t)|^2$ , which reads

$$\begin{aligned} I(t) = & |\mathcal{E}(t)|^2 = \sum_{p,r} A_{p,1} A_{r,1}^* e^{i(p-r)\omega_{rep,1}t} \\ & + \sum_{p,r} A_{p,2} A_{r,2}^* e^{i(p-r)\omega_{rep,2}(t+\Delta t)} \\ & + e^{-i\omega_c\Delta t} \sum_{n,m} A_{n,1} A_{m,2}^* e^{i(n\omega_{rep,1} - m\omega_{rep,2})t + im\omega_{rep,2}\Delta t} \\ & + e^{i\omega_c\Delta t} \sum_{n,m} A_{n,1}^* A_{m,2} e^{-i(n\omega_{rep,1} - m\omega_{rep,2})t - im\omega_{rep,2}\Delta t}. \end{aligned} \quad (21)$$



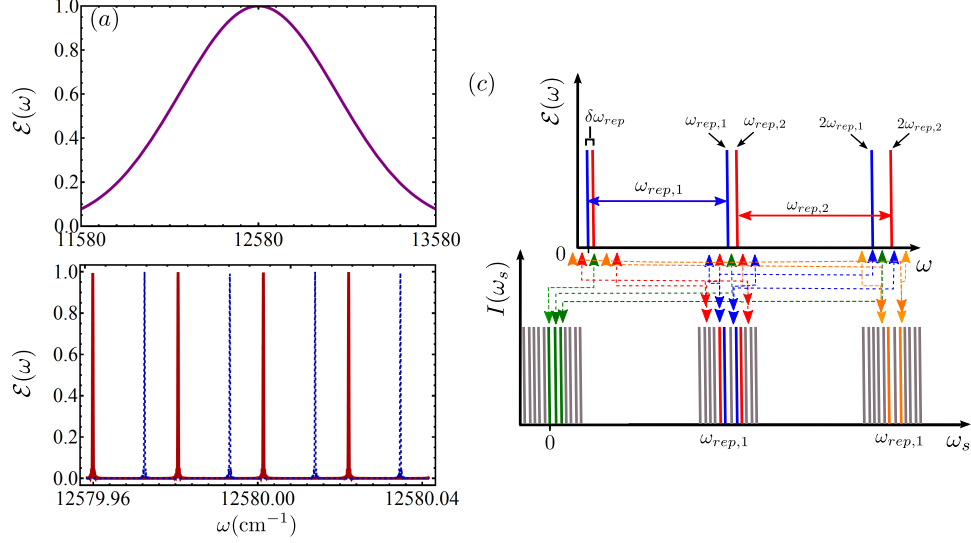


FIG. 4: (Color online)(a) Frequency comb, Eq. (19), for a Gaussian envelope Eq. (20)  $\omega_{rep,1} = 0.0033\text{cm}^{-1}$ ,  $\eta = 10^{-6}$ ,  $\omega_c = 12580\text{cm}^{-1}$ , and  $\sigma = 441\text{cm}^{-1}$ . (b) The dual comb in (a) is displayed on a much smaller scale to shown the individual comb lines of comb 1 (blue) and comb 2 (red). (c) Schematic of  $\mathcal{E}(\omega)$  for the dual freq comb Eq. (19). (d) Interferogram of the double comb Eq. (22) is shown for the first three frequency combs resulting from the beating of two frequency combs in the time domain.

The last two terms in Eq. (21) contain many possible beat frequencies:  $n\omega_{rep,1} - m\omega_{rep,2}$ . The Fourier transform of Eq. (21) reads

$$I(\omega_s) = \int dt I(t) e^{i\omega_s t}. \quad (22)$$

For  $n = m$ , Eq. (22) will give a frequency comb  $\sum_n \delta(\omega - n\delta\omega_{rep})$ . The application of a second comb, thus down-converts comb 1 by the factor

$$\eta = \delta\omega_{rep}/\omega_{rep,1}. \quad (23)$$

This frequency comb has line spacing  $\delta\omega_{rep}$  and has envelope is the product of the envelopes of the two fields.

The dual frequency comb, Eq. (19) is sketched in Fig. (4)(c). Fig. (4)(d) sketches the Fourier transform of the interferometric signal Eq. (21) given by Eq. (22). The first group of lines corresponds to the selection of the modes  $n = m$ . The second group corresponds to  $m = n + 1$  and has the form  $\sum_n \delta(\omega_s - \omega_{rep,2} - n\delta\omega_{rep})$ . It is centered at  $\omega_s \approx \omega_{rep,1}$  with line spacing

$\delta\omega_{rep}$  and is identical to the first group. The third group is at  $\omega_s \approx 2\omega_{rep,1}$  and corresponds to the combination  $m = n + 2$ . The spectrum contains an infinite number of identical frequency combs center at  $\omega_s \approx p\omega_{rep,1}$ , where  $p$  is an integer. Typically the only the first group of lines is measured and the higher frequencies can be cut-off experimentally by using a low-pass filter in the acquisition circuit[4]. For two combs with THz carrier frequencies, and repetition frequencies  $\omega_{rep,1} = 2\pi 100$  MHz,  $\delta\omega_{rep} = 2\pi 100$  Hz, the peaks in the spectrum are multiplied by  $\eta = 10^{-6}$  and the spectrum lies in the radiofrequency regime[4]. For unambiguous assignment of the comb modes, the bandwidth should not exceed  $\pm\omega_{rep,1}/2$ , which can be derived from the Nyquist theorem.

## V. COMB LINE SELECTION IN THE NONLINEAR TIME-RESOLVED TRANSMISSION SIGNAL WITH SCALING $\tilde{\mathcal{E}}_1^2\tilde{\mathcal{E}}_2^2$

The time-resolved transmission spectrum for two frequency combs contains the signal  $\tilde{\mathcal{E}}_1^2\tilde{\mathcal{E}}_2^2$ ,  $\tilde{\mathcal{E}}_1^3\tilde{\mathcal{E}}_2$  and  $\tilde{\mathcal{E}}_1\tilde{\mathcal{E}}_2^3$ . We analyze the spectrum separately for  $\tilde{\mathcal{E}}_1^2\tilde{\mathcal{E}}_2^2$  and  $\tilde{\mathcal{E}}_1^3\tilde{\mathcal{E}}_2$ . The expression for the spectrum scaling as  $\tilde{\mathcal{E}}_1\tilde{\mathcal{E}}_2^3$  are similar to  $\tilde{\mathcal{E}}_1^3\tilde{\mathcal{E}}_2$  with the  $\delta\omega_{rep} \rightarrow -\delta\omega_{rep}$ .

We select terms that scale as  $\tilde{\mathcal{E}}_1^2\tilde{\mathcal{E}}_2^2$ . Fourier transform of interferometric signal with two interactions from comb 1 and 2, gives the following possible beat frequencies

$$\begin{aligned}\omega_s &= (n - r)\omega_{rep,1} + (m - p)\omega_{rep,2}, \\ &= (n + r)\omega_{rep,1} - (m + p)\omega_{rep,2}, \\ &= (n - r)\omega_{rep,1} - (m - p)\omega_{rep,2}.\end{aligned}\tag{24}$$

Note that the exchange of  $\omega_{rep,1}$  and  $\omega_{rep,2}$  is possible in Eq. (24). The two interactions with comb 1 correspond the indices  $r$  and  $n$ , and two interactions with comb 2 to  $p$  and  $m$ . Similar to the interferometric signal Eq. (21), the relation  $m - p = r - n$ , for the first term in Eq. (24), will give a frequency comb  $\sum_{n,r} \delta((n - r)\delta\omega_{rep} - \omega_s)$ . The combination  $m - p = r - n + 1$  will give identical frequency comb  $\sum_{n,r} \delta((n - r)\delta\omega_{rep} + \omega_{rep,2} - \omega_s)$ , centered at  $\omega_s \approx \omega_{rep,1}$ . Based on this observation, we use a delta-function to select the correct combination of line numbers. For example, the combination of the line numbers in Eq. (24), will acquire the corresponding

delta-functions

$$\begin{aligned}
&\delta(n - r + m - p), \\
&\delta(n + r - m - p), \\
&\delta(n - r - m + p),
\end{aligned} \tag{25}$$

respectively. When expanding the field correlation functions we can insert the corresponding delta-function and eliminate one of the summations over the spectral line numbers. This is done in Appendix A and the final expression for the time-resolved transmission spectrum is given in Eq. (A3).

The time-resolved transmission spectrum  $S_t(\omega_s)$ , Eq. (A3) contains many peaks. The TPA and Raman peaks that do not depend on  $n$  or  $m$ :

$$\begin{aligned}
\omega_s &= \pm\eta\omega_{f_1g_1}, \\
\omega_s &= \pm\eta\omega_{g_2g_1}.
\end{aligned} \tag{26}$$

Other peaks that depend upon  $n$  and  $m$  and that lie within the displayed regime  $\pm\omega_{rep,1}/2$  are

$$\begin{aligned}
\tilde{\omega}_{f_1g_1}^+ &= \eta(\omega_{f_1g_1} - (m + n)\omega_{rep,1}) \\
\tilde{\omega}_{e_1g_1}^+ &= \eta(\omega_{e_1g_1} - n\omega_{rep,1}) \\
\tilde{\omega}_{e_1g_1}^- &= -\eta(\omega_{e_1g_1} + n\omega_{rep,1}) \\
\tilde{\omega}_{g_2g_1}^+ &= \eta(\omega_{g_2g_1} - (m + n)\omega_{rep,1}) \\
\tilde{\omega}_{g_2g_1}^- &= -\eta(\omega_{g_2g_1} + (m + n)\omega_{rep,1}).
\end{aligned} \tag{27}$$

The peaks  $\omega_s = -\eta(\omega_{f_1g_1} + (m + n)\omega_{rep,1})$ ,  $\omega_{e_1g_1} \pm n\omega_{rep,1}$ ,  $\omega_{g_2g_1} + (m + n)\omega_{rep,1}$  lie outside the displayed regime. The center position of the peaks that depend on  $n$  and  $m$  can be found by substituting  $n = m = \omega_c/\omega_{rep,1}$ . The single-photon peaks  $\tilde{\omega}_{e_1g_1}^-$  and  $\tilde{\omega}_{e_1g_1}^+$  depend  $n$ ; while, the range of  $n$  depends upon the width of the frequency comb. Hence, the width of these peaks will be close to the width of the frequency comb multiplied by  $\eta$ . The TPA and Raman resonances depend on  $m$  and  $n$ , so that these peaks will be twice as broad as the single-photon peaks.

The down shifting the peaks can be understood by comparing Eqs. (8) and (11). Eq. (8) contains an  $\omega'$  integration, which is a result of the time resolved signal detection. This integration mixes the frequency combs and shifts the peaks into the radiofrequency range. Using the delta function in Eq. (8), and inserting it into the field  $\tilde{\mathcal{E}}^*(\omega' - \omega_s)$ , we find  $\mathcal{E}^*(\omega_1 + \omega_2 - \omega_3 - \omega_s)$ ,

which mixes the four frequencies in the diagrams of Fig. 2. In Eq. (11), using the delta function we have  $\mathcal{E}^*(\omega_1 + \omega_2 - \omega_3)$ , which mixes three of the frequencies.

The modulation of the transmission signal in the radiofrequency range, can be seen from the expression Eq. (A3), which is proportional to

$$\begin{aligned}
S_{t1122}^{(3)}(\omega_s; \omega_{rep,1}, \omega_{rep,2}, \tau_2) &\propto -\mathcal{I} \frac{2}{2\pi\hbar} \omega_{rep,1}^2 \omega_{rep,2}^2 \left[ \tilde{\mathcal{E}}_2^*(m\omega_{rep,2} - \omega_c) \tilde{\mathcal{E}}_1(n\omega_{rep,1} - \omega_c) \tilde{\mathcal{E}}_2^*(p\omega_{rep,2} - \omega_c) \right. \\
&\times \tilde{\mathcal{E}}_1(r\omega_{rep,1} - \omega_c) V_{g_1e_1} V_{e_1f_1} V_{f_1e_1} V_{e_1g_1} \\
&\times \frac{\delta((r+n)\omega_{rep,1} - (p+m)\omega_{rep,2} - \omega_s)}{(r\omega_{rep,1} - \omega_{e_1g_1} + i\Gamma_{e_1})((n+r)\omega_{rep,1} - \omega_{f_1g_1} + i\Gamma_{f_1})((n+r)\omega_{rep,1} - p\omega_{rep,2} - \omega_{e_1g_1} - i\Gamma_{e_1})} \\
&+ \tilde{\mathcal{E}}_1^*(n\omega_{rep,1} - \omega_c) \tilde{\mathcal{E}}_2(m\omega_{rep,2} - \omega_c) \tilde{\mathcal{E}}_2^*(p\omega_{rep,2} - \omega_c) \tilde{\mathcal{E}}_1(r\omega_{rep,1} - \omega_c) V_{g_2e_1} V_{e_1g_1} V_{g_1e_1} V_{e_1g_2} \\
&\times \left. \frac{\delta((r-n)\omega_{rep,1} - (p-m)\omega_{rep,2} - \omega_s)}{(r\omega_{rep,1} - \omega_{e_1g_1} + i\Gamma_{e_1g_1})((p-m)\omega_{rep,2} - \omega_{g_2g_1} - i\Gamma_{g_2g_1})(p\omega_{rep,2} - \omega_{e_1g_1} - i\Gamma_{e_1g_1})} \right]. \tag{28}
\end{aligned}$$

The  $\tilde{\mathcal{E}}_1^2 \tilde{\mathcal{E}}_2^2$  scaling signal is designated as 1122. The first term

$$S_{t1122}^{(3)}(\omega_s) \propto \frac{\delta((r+n)\omega_{rep,1} - (p+m)\omega_{rep,2} - \omega_s)}{((n+r)\omega_{rep,1} - \omega_{f_1g_1} + i\Gamma_{f_1})}, \tag{29}$$

gives the two-photon peaks multiplied by  $\eta$ . Using  $n+r = m+p$  in the delta-function gives  $(n+r)\delta\omega_{rep} = \omega_s$ . Substituting  $(n+r) = \omega_s/\delta\omega_{rep}$  into the denominator yields the TPA resonance at  $\omega_s = \eta\omega_{f_1g_1}$ . A similar effect occurs for the second term with the Raman resonances. From the combination of the terms

$$S_{t1122}^{(3)}(\omega_s) \propto \frac{\delta((r-n)\omega_{rep,1} - (p-m)\omega_{rep,2} - \omega_s)}{((p-m)\omega_{rep,2} - \omega_{g_2g_1} - i\Gamma_{g_2g_1})}, \tag{30}$$

the selection  $r-n = p-m$  in the delta function gives  $(p-m)\delta\omega_{rep} = \omega_s$ . Substituting this combination into dominator, we find the Raman resonance at  $\omega_s = \eta\omega_{g_2g_1}$ .

Two rather large summations are required to evaluate in the time-resolved transmission signal Eq. (A3). We performed them using the Monte Carlo method[40, 41], where we randomly sample the comb line numbers in the frequency comb. Convergence is verified by changing the sample number and observing changes in the spectra.

The repetition frequency is selected as  $\omega_{rep,1} = 0.080\text{cm}^{-1}$ , so that the TPA peaks can be observed within the range  $\pm\omega_{rep,1}/2$ . The peaks in the transmission spectra are multiplied by the factor  $\eta = 10^{-6}$ , which is in the radiofrequency range. We use a Gaussian envelope Eq. (20) with  $\sigma = 1.8 * 10^6\text{cm}^{-1}$ .

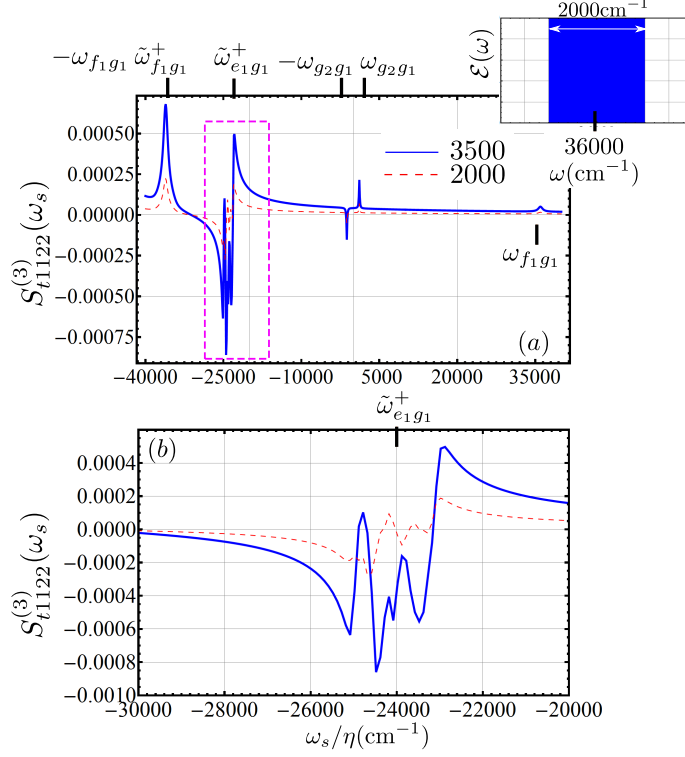


FIG. 5: (Color online) (a) The resonant time-resolved transmission spectrum from Eq. (A3) is plotted. Inset shows an illustration of frequency comb used,  $\omega_c = 36000\text{cm}^{-1}$  and width  $2000\text{cm}^{-1}$ . (b) The spectrum in the purple region near  $\omega_s = \tilde{\omega}_{e1g1}^+$  is enlarged. The expression for the peaks are given in Eqs. (26), (27).

The resonant time-resolved transmission signal Eq. (A3) is displayed in Fig. 5(a), for  $\Delta t = 0$ , and  $\omega_c = 36000\text{cm}^{-1}$ . The frequency comb range was selected as  $\omega = (35000\text{cm}^{-1}, 37000\text{cm}^{-1})$  and contains 25,000 comb lines. The range was randomly sampled for 2,000 pulses (dashed-red) or 3,500 pulses (solid-blue).  $S_{t1122}^{(3)}(\omega_s)$  is in the units  $\frac{2\pi}{h}(\frac{1}{2\pi\hbar})^3\omega_{rep,1}^4 E_1^2 E_2^2$  with the dipole moments set to one. The inset shows an illustration of the frequency comb used. The spectrum shows the TPA and Raman resonances at  $\omega_s = \pm\eta\omega_{f1g1}$  and  $\omega_s = \pm\eta\omega_{g2g1}$ , respectively. The  $\omega_s = \tilde{\omega}_{e1g1}^+$  peak is centered at  $\omega_s = \eta(\omega_{e1g1} - \omega_c) = -24000\eta\text{cm}^{-1}$  has a width  $\approx 2000\eta\text{cm}^{-1}$ . The  $\omega_s = \tilde{\omega}_{f1g1}^+$  peak is located at  $\omega_s = \eta(\omega_{f1g1} - 2\omega_c) = -36000\eta\text{cm}^{-1}$ . Since its position depends on both  $n$  and  $m$  it will have a width of  $\approx 4000\eta\text{cm}^{-1}$ . This is the reason why the negative two-photon peak in Fig. 5(a) is more pronounced than the positive peak.

The shaded region in Fig. 5(a) is re-plotted in Fig. 5(b) on a larger scale, which corresponds to  $\omega_s = \tilde{\omega}_{e1g1}^+$ . We see that the width of the peak is  $\approx 2000\eta\text{cm}^{-1}$  and that it contains both

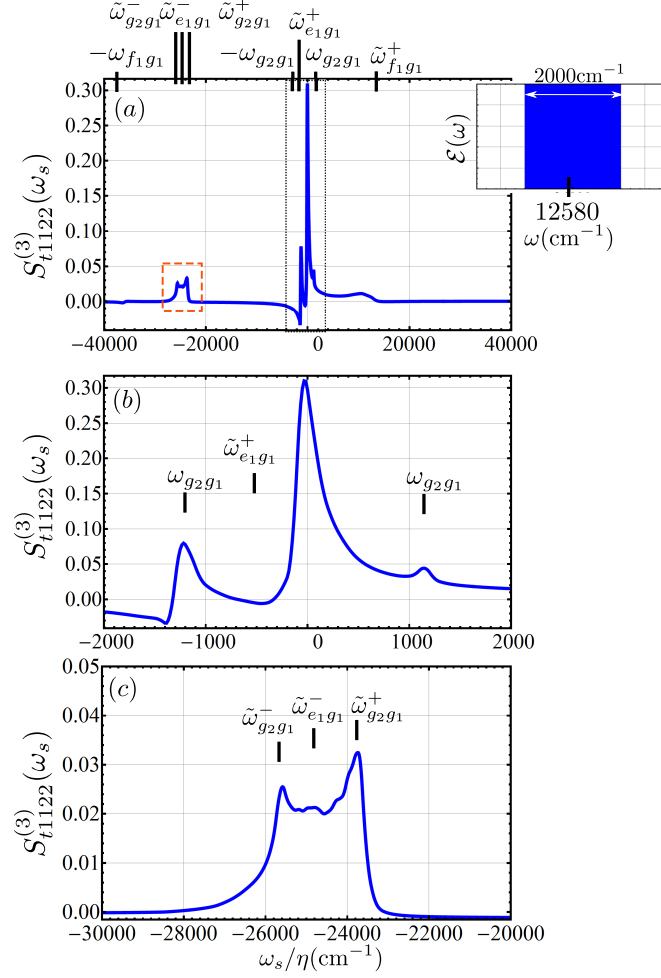


FIG. 6: (Color online) (a) The off-resonant time-resolved transmission spectrum. Inset shows a frequency comb centered at  $\omega_c = 12580 \text{ cm}^{-1}$ . (b) The spectrum for the green region about  $\omega_s = 0$  is enlarged. (c) The spectrum for the pink region near  $\omega_s = \tilde{\omega}_{e1g1}^-$  is enlarged. The expression for the peaks are given in Eqs. (26), (27).

absorption and emission features. Comparing the dashed-red for 2,000 sampled pulses to the solid-blue 3,500 pulses, we see the same features demonstrating that the data for the 2,000 sampled pulses represents the spectrum.

The spectrum for  $\omega_s > 0$  in Fig. 5(a), in the radiofrequency range, contains only the Raman and TPA peaks. Compared to the frequency-dispersed transmission spectra Fig. 3(c). Only the vibrational and TPA peaks are present in Fig. 5(b), while the Stokes, Rayleigh, and TPA peaks are present in Fig. 3(c). In Figs. 5(a), 3(d), the single-photon peaks are shifted by  $\eta\omega_c$  or  $\omega_c$  and there are Raman resonances not shifted by  $\eta\omega_c$  or  $\omega_c$ . In Fig. 5(a) there are TPA resonances that are not

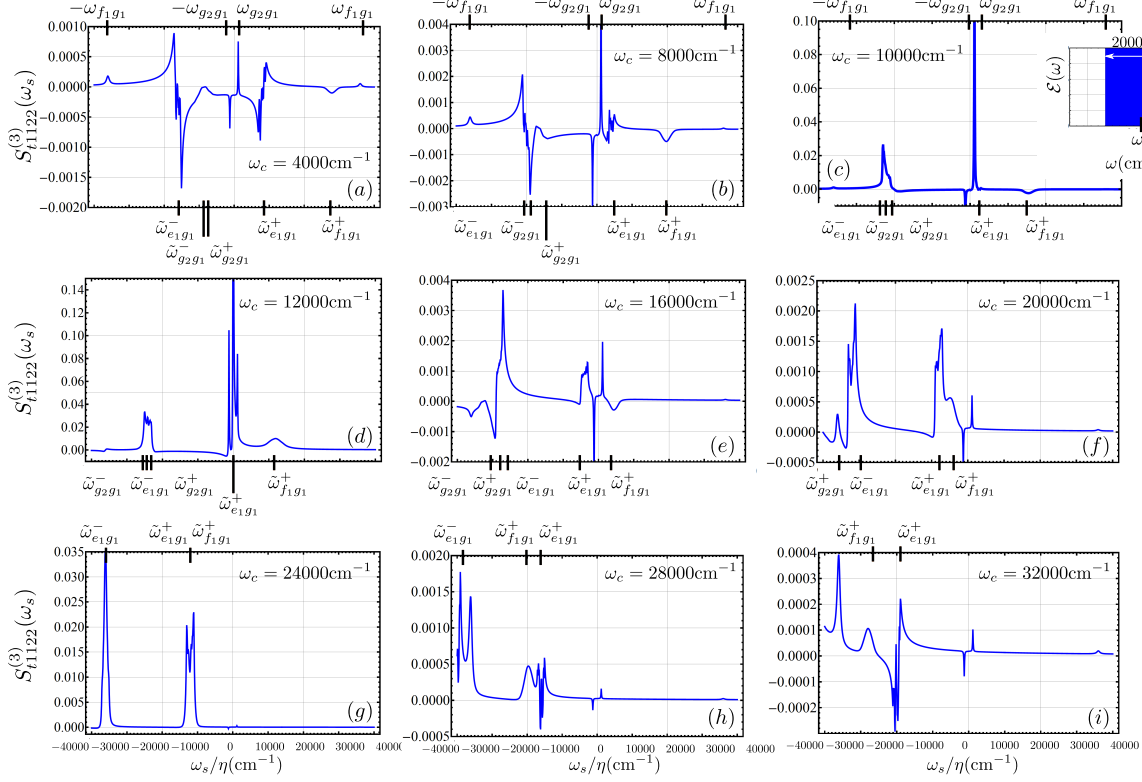


FIG. 7: (Color online) The time-resolved transmission spectrum  $S_{t1122}^{(3)}(\omega_s)$  Eq. (A3) is displayed, for various values of  $\omega_c$ . The inset shows the frequency comb centered at  $\omega_c$  and width  $2000\text{cm}^{-1}$ . The expression for the peaks are given in Eqs. (26), (27).

shifted by  $\eta\omega_c$ , while in Fig. 3(d), they are shifted by  $2\omega_c$ .

The off-resonant transmission spectrum Eq. (A3) is shown in Fig. 6(a) for  $\omega_c = 12580\text{cm}^{-1}$ . The frequency comb range was selected as  $\omega = (11580\text{cm}^{-1}, 13580\text{cm}^{-1})$  and contains 25,000 comb lines. The range was randomly sampled for 2,000 pulses. The TPA peaks are very weak. The spectrum is composed of Raman resonances at  $\omega_s = \pm\eta\omega_{g2g1}$ ,  $\tilde{\omega}_{g2g1}^+$ ,  $\tilde{\omega}_{g2g1}^-$ , single-photon peaks at  $\omega_s = \tilde{\omega}_{e1g1}^+$ ,  $\tilde{\omega}_{e1g1}^-$ , a TPA at  $\omega_s = \tilde{\omega}_{f1g1}^+$ ,  $-\eta\omega_{f1g1}$  and a peak at  $\omega_s = 0$ . The peak at  $\omega_s = \tilde{\omega}_{f1g1}^+ = 10840\eta\text{cm}^{-1}$  has a width of  $\approx 4000\eta\text{cm}^{-1}$ .

The region in the pink shaded area near  $-24000\eta\text{cm}^{-1}$  is re-plotted in Fig. 6(c) on an expanded scale and shows the combination of the peaks  $\omega_s = \tilde{\omega}_{e1g1}^-$ ,  $\tilde{\omega}_{g2g1}^+$ , and  $\tilde{\omega}_{g2g1}^-$ , centered at  $\omega_s = -24580, -23960, -26360\eta\text{cm}^{-1}$ , respectively.

The green shaded area in Fig. 6(a), is replotted in Fig. 6(b). Compared to the resonant transmission spectrum Fig. 5(a), there is an additional peak at  $\omega_s = 0$ . This peak originates from the  $\omega_s = (\omega_{e1g1} - n\omega_{rep,1})$ , which is not multiplied by the factor  $\eta$ . For  $\omega_{e1g1} = n\omega_{rep,1}$ , there is

a peak which is located within the regime  $\omega_{rep,1}/2$  at zero. The  $\omega_s = \tilde{\omega}_{e_1g_1}^+$  peak is centered at  $\tilde{\omega}_{e_1g_1}^+ = -580\eta\text{cm}^{-1}$ , with width  $\approx 2000\eta\text{cm}^{-1}$ .

The spectrum for  $\omega_s > 0$  in Fig. 6(b) contains only the Raman peak. This plot can be compared to the experimental results of Ref. [4]. The spectrum shows qualitative agreement with there findings for measuring the off-resonant time-resolved transmission spectrum, without the peak at zero, which originates from the single-photon peak  $\omega_s = (\omega_{e_1g_1} - n\omega_{rep,1})$ . Note that we selected a repetition frequency and level scheme Fig. 1 than Refs. [4].

The time-resolved transmission spectrum for various values of  $\omega_c$  are plotted in Fig. 7. The inset shows the frequency comb that we use with width  $2000\text{cm}^{-1}$ . The two large summations in Eq. (A3) are done by randomly sampling the range with 2,000 pulses. The transmission spectrum for  $\omega_c = 4000\text{cm}^{-1}$  is shown in Fig. 7(a). It contains the two-photon and Raman resonances at  $\omega_s = \pm\eta\omega_{f_1g_1}, \pm\eta\omega_{g_2g_1}$  and the five peaks in Eq. (27). The  $\omega_s = \tilde{\omega}_{e_1g_1}^+$  and  $\tilde{\omega}_{e_1g_1}^-$  peaks contain both absorption and emission features. The Raman peaks at  $\omega_s = \tilde{\omega}_{g_2g_1}^+$  and  $\tilde{\omega}_{g_2g_1}^-$  interfere. The  $\omega_s = \tilde{\omega}_{f_1g_1}^+$  peak is an absorption peak. Increasing  $\omega_c = 8000\text{cm}^{-1}$ , in Fig. 7(b), shifts the five peaks in Eq. (27) toward the left. In Fig. 7(c), for  $\omega_c = 10000\text{cm}^{-1}$  the  $\omega_s = \tilde{\omega}_{e_1g_1}^+$  overlaps the  $\omega_s = \pm\eta\omega_{g_2g_1}$  peak and amplifies the peak.

In the Fig. 7(d), for  $\omega_c = 12000\text{cm}^{-1}$ , there is peak located at zero, corresponding to  $\omega_s = (\omega_{e_1g_1} - n\omega_{rep,1})$ , which is not multiplied by the factor  $\eta$ . This peak only occurs for  $\omega_{e_1g_1} = n\omega_{rep,1} = \omega_c$ . In addition, the peak  $\omega_s = \tilde{\omega}_{e_1g_1}^+$  is located at zero. Increasing  $\omega_c$  further, in Fig. 7(f), the  $\omega_s = \tilde{\omega}_{g_2g_1}^-$  position becomes located beyond the detected regime and all peaks from Eq. (27) are located in the regime  $\omega_s < 0$ . In Fig. 7(g), the  $\tilde{\omega}_{e_1g_1}^-$  peak overlaps the TPA at  $\omega_s = -\omega_{f_1g_1}$ , amplifying the TPA. Increasing  $\omega_c$  further, it is possible to shift the location of the  $\omega_s = \tilde{\omega}_{g_2g_1}^+$  and  $\tilde{\omega}_{e_1g_1}^-$  beyond the detected regime, as in Fig. 7(i).

## VI. TIME-RESOLVED TRANSMISSION SIGNAL WITH SCALING $\tilde{\mathcal{E}}_1^3 \tilde{\mathcal{E}}_2$

Selection of three interactions with comb 1 and one interaction with comb 2 will give the down-converted single-photon resonances, which do not depend upon the comb line number. The Fourier



transform of the interferometric signal will give the following beat frequencies

$$\begin{aligned}
\omega_s &= (n - r + m)\omega_{rep,1} - p\omega_{rep,2}, \\
&= (n + r - m)\omega_{rep,1} - p\omega_{rep,2}, \\
&= (n - r - m)\omega_{rep,1} + p\omega_{rep,2}.
\end{aligned} \tag{31}$$

Similar to the methods used in Sec. V, We will make use a delta function to select the correct combination of line numbers in the transmission signal. The transmission spectrum Eq. (B3) is derived in Appendix B. The peaks in the transmission signal are

$$\begin{aligned}
\omega_{e_1g_1} &= \pm\eta\omega_{e_1g_1} \\
\Omega_{f_1g_1}^+ &= \eta(\omega_{f_1g_1} - m\omega_{rep,1}) \\
\Omega_{f_1g_1}^- &= -\eta(\omega_{f_1g_1} - n\omega_{rep,1}) \\
\Omega_{e_1g_1}^+ &= \eta(\omega_{e_1g_1} + (n - m)\omega_{rep}) \\
\Omega_{e_1g_1}^- &= -\eta(\omega_{e_1g_1} - (n - m)\omega_{rep}) \\
\Omega_{g_2g_1}^+ &= \eta(\omega_{g_2g_1} + n\omega_{rep}) \\
\Omega_{g_2g_1}^- &= -\eta(\omega_{g_2g_1} + m\omega_{rep}).
\end{aligned} \tag{32}$$

The center position of the peaks can be found by substituting  $n = \omega_c/\omega_{rep,1}$  and  $m = \omega_c/\omega_{rep,1}$  into Eq. (32). The peak  $\Omega_{e_1g_1}^\pm$  is centered at  $\pm\omega_{e_1g_1}$ . The peak positions  $\Omega_{f_1g_1}^\pm$  are shifted by  $-\eta\omega_c$ , while, the peaks  $\Omega_{g_2g_1}^\pm$  are shifted by  $\eta\omega_c$ . Comparing to the peaks in Fig. 3, the TPA peaks and Raman peaks in Fig. 3(c),  $\mathcal{S}_f(\omega)$ , are shifted by  $\omega_c$ , while the single-photon peaks are not shifted by  $\omega_c$ .

The down-conversion of the single photon peaks can be seen from the transmission signal Eq. (B3), which is proportional to

$$\begin{aligned}
S_{t1112}^{(3)}(\omega_s; \omega_{rep,1}, \omega_{rep,2}, \tau_2) &\propto -\mathcal{I} \frac{2}{2\pi\hbar} \omega_{rep,1}^3 \omega_{rep,2} \left[ \tilde{\mathcal{E}}_1^*(m\omega_{rep,1} - \omega_c) \tilde{\mathcal{E}}_1(n\omega_{rep,1} - \omega_c) \tilde{\mathcal{E}}_2^*(r\omega_{rep,1} - \omega_c) \right. \\
&\times \tilde{\mathcal{E}}_1(p\omega_{rep,2} - \omega_c) V_{g_1e_1} V_{e_1g_2} V_{g_2e_1} V_{e_1g_1} \\
&\times \frac{\delta((n - r - m)\omega_{rep,1} + p\omega_{rep,2} - \omega_s)}{(p\omega_{rep,2} - \omega_{e_1g_1} + i\Gamma_{e_1})(p\omega_{rep,2} - r\omega_{rep,1} - \omega_{g_2g_1} + i\Gamma_{g_2})((n - r)\omega_{rep,1} + p\omega_{rep,2} - \omega_{e_1g_1} - i\Gamma_{e_1})} \Big],
\end{aligned} \tag{33}$$

The index 1112 represents the signal scaled as  $\tilde{\mathcal{E}}_1^3 \tilde{\mathcal{E}}_2$ . Equation (33) is proportional to

$$S_{t1112}^{(3)}(\omega_s; \omega_{rep,1}, \omega_{rep,2}, \tau_2) \propto \frac{\delta((n - r - m)\omega_{rep,1} + p\omega_{rep,2} - \omega_s)}{(p\omega_{rep,2} - \omega_{e_1g_1} + i\Gamma_{e_1})}. \tag{34}$$

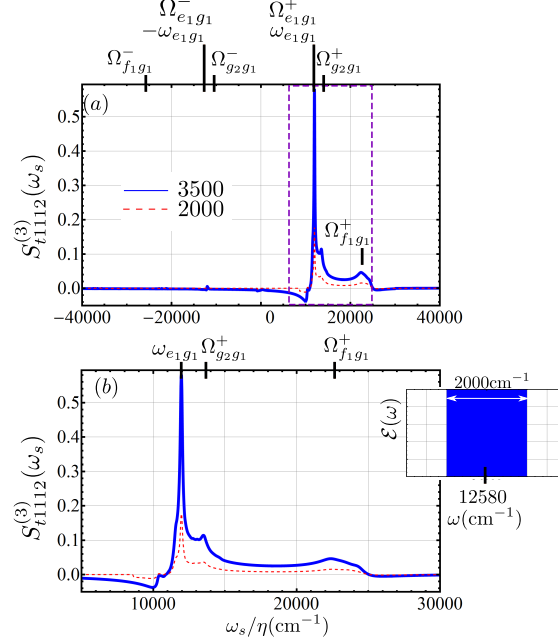


FIG. 8: (Color online) (a) The time-resolved transmission signal for three interactions with comb 1, Eq. (B3) is plotted. The inset shows an illustration of the frequency comb used,  $\omega_c = 1258\text{cm}^{-1}$ . The peaks in the spectrum are given by Eq. (32). (b) The spectrum in the purple region is re-plotted.

The selection  $n - r - m = -p$  from the measurement of interferometric signal gives  $p = -\omega_s/\delta\omega_{rep}$ . Substituting this into the dominator we find the single-photon resonance at  $\omega_s = -\eta\omega_{e_1 g_1}$ .

The two large summations in the transmission signal  $S_{t1112}^{(3)}(\omega_s)$  are calculated using the Monte Carlo method, as in Sec. V. We used the same values for the repetition frequency and Gaussian pulse width as in Sec. V. The off-resonant transmission signal is displayed for  $\omega_c = 12580\text{cm}^{-1}$  and a frequency comb width  $\omega = (11580\text{cm}^{-1}, 13580\text{cm}^{-1})$  in Fig. 8. The inset shows an illustration of the frequency comb used. The range was randomly sampled for 2,000 pulses (dashed-red) and 3,500 pulses (solid-blue).  $S_{t1112}^{(3)}(\omega_s)$  is in the units  $\frac{2\pi}{h}(\frac{1}{2\pi h})^3\omega_{rep,1}^4 E_1^3 E_2$  with the dipole moments set to one. The transmission spectrum in Fig. 8(a) is dominated by the  $\omega_s = \omega_{e_1 g_1}$  peak. The  $\omega_s = \Omega_{e_1 g_1}^+$  peak has a width of  $4000\eta\text{cm}^{-1}$  and overlaps the  $\omega_s = \omega_{e_1 g_1}$  peak. The  $\omega_s = \Omega_{f_1 g_1}^+$  peak has a width of  $2000\eta\text{cm}^{-1}$ . Comparing the 2,000 sampled to the 3,500 sampled, the features from the 2,000 pulse resemble the 3,500. The purple region is replotted in Fig. 8(b) on a smaller regime. The  $\omega_s = \Omega_{g_2 g_1}^+$  has a width of  $2000\text{cm}^{-1}$ . There is a feature near  $\omega_s = -10,000\eta\text{cm}^{-1}$

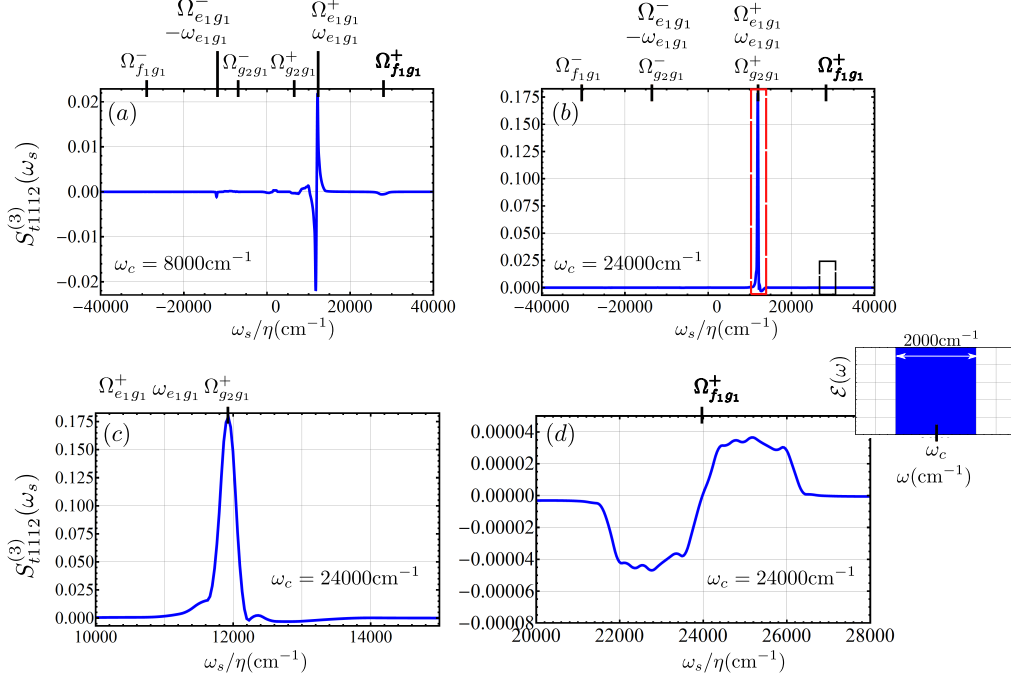


FIG. 9: (Color online) The time-resolved transmission signal for three interactions with comb 1, Eq. (B3) is plotted for two values of  $\omega_c$ : (a)  $\omega_c = 80000\text{cm}^{-1}$ , (b)  $\omega_c = 240000\text{cm}^{-1}$ . The inset shows an illustration of the frequency comb used. The peaks in the spectrum given by Eq. (32). (c) The spectrum in the purple region of (b) is re-plotted. (d) The spectrum in the green region of (b) is re-plotted.

that corresponds to the  $\omega_s = \Omega_{e_1g_1}^+$  peak.

The transmission signal for two values of  $\omega_c$  are shown in Fig. 9. For  $\omega_c < \omega_{e_1g_1}$  in Fig. 9(a), the spectrum is mostly composed of the single-photon peak, which shows both emission and absorption features. For  $\omega_c > \omega_{e_1g_1}$ , in Fig. 9(b), the single-photon peak becomes an emission peak and all peaks dependent upon comb line number are suppressed. There are three peaks,  $\omega_s = \omega_{e_1g_1}, \Omega_{g_2g_1}^+, \Omega_{e_1g_1}^+$  that overlap at the single-photon resonance. The purple region is replotted in Fig. 9(c), showing that the single-photon resonance has width according to the dephasing rate. The peak at  $\Omega_{f_1g_1}^+$ , the green region in Fig. 9(b) is replotted in Fig. 9(d).

## VII. TIME-RESOLVED TRANSMISSION SPECTRA WITH SHAPED SPECTRAL PHASE

The future developments in spectroscopy using the frequency comb include shaping the individual pulses in the pulse train. This method requires a pulse shaper to have a spectral resolu-

tion that matches the spacing of the comb lines of the input pulse train. This was demonstrated recently[25, 27, 29–31]. Currently, this method is limited to small frequency combs, say 100 comb lines. Generation of pulse shaping in dual comb Fourier transform spectroscopy was recently demonstrated for triangular shaped pulses[26]. The two frequency combs contained 4 identically shaped-pulses with slightly different repetition rates. Here, we consider pulse-shaping of a frequency comb with 25,000 pulses using a sinusoidal spectral phase function. This was demonstrated in Doppler free spectroscopy[6] with a repetition frequency of 180 MHz ( $0.06\text{cm}^{-1}$ ).

The spectrum with two interactions with comb 1  $S_{t1122}^{(3)}(\omega)$  contains the peaks  $\omega_s = \pm\eta\omega_{g_2g_1}$  and  $\omega_s = \pm\eta\omega_{f_1g_1}$ , which are independent of the comb line numbers. We are interested in controlling these resonances by means of employee an oscillating phase onto the pulse envelope

$$\tilde{\mathcal{E}}_1(\omega) = \mathcal{E}_1(\omega)e^{i\phi(\omega)}, \quad \tilde{\mathcal{E}}_2(\omega) = \mathcal{E}_2(\omega)e^{i\phi(\omega)}, \quad (35)$$

where  $\mathcal{E}_1(\omega)$  and  $\mathcal{E}_2(\omega)$  represent the real part, which is a Gaussian, Eq. (20). The sinusoidal spectral phase reads

$$\phi(\omega) = \alpha \sin(\beta\omega + \Phi), \quad (36)$$

where  $\alpha$  is the modulation depth,  $\beta$  is inverse modulation frequency and  $\Phi$  is the modulation phase. A cosine spectral phase occurs when  $\Phi = \pi/2$ . Adding an oscillating phase alters the temporal profile, breaking each pulse into a train of sub-pulses.

In Fig. 10(a), we show the time-resolved transmission spectrum, without an oscillating phase, for  $\omega_c = 36000\text{cm}^{-1}$  and width  $\omega = (35000\text{cm}^{-1}, 37000\text{cm}^{-1})$ . See the inset. For an even spectral phase Fig. 10(b),  $\Phi = \pi/2$ , both the Raman and TPA peaks are present. However, for an odd spectral phase Fig. 10(c),  $\Phi = 0$ , only the Raman peak is present.

Suppression of the Raman peak can be done by selection of the modulation frequency  $\beta$ . In Fig. 11(a), for an even phase function, the Raman peak in the spectrum is minimized while the TPA peak is enhanced. The minimization of the Raman peak is not do to a minimum in the oscillating spectral phase function. This is verified in Fig. 11(b), where we plot the transmission spectrum with an odd phase function  $\Phi = 0$ . The inset, which is a plot of (c) and (d), demonstrates that the cosine and sine spectral phase functions are out of phase.

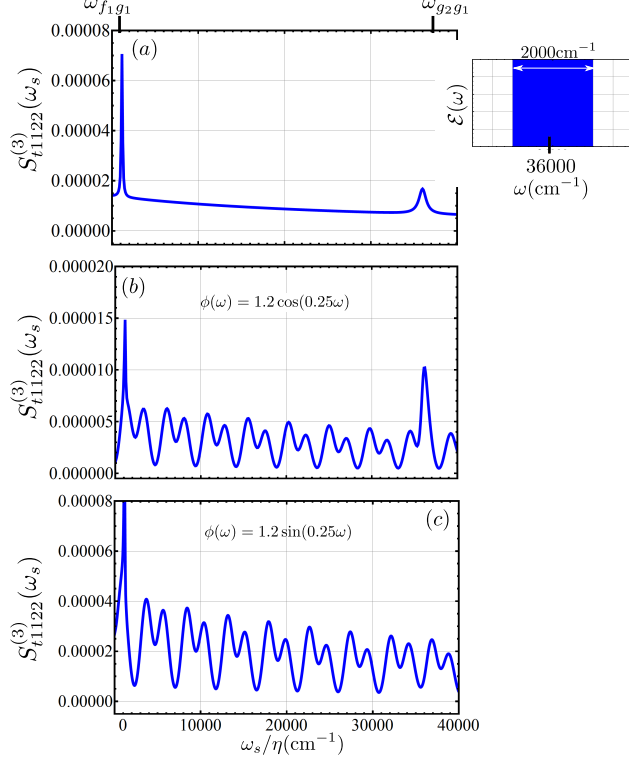


FIG. 10: (Color online) (a) The resonant time-resolved transmission signal Eq. (A3) without a sinusoidal phase. The resonant transmission signal Eq. (A3) using Eq. (35), with an oscillating phase Eq. (36), for  $\beta = 0.25$ ,  $\alpha = 1.2$ , and two different values of the  $\Phi$ ; (a)  $\Phi = \pi/2$ ; (b)  $\Phi = 0$ . The inset in (a) shows the frequency comb used.

### VIII. SUMMARY

We have shown that dual comb spectroscopy can be described as the time-resolved transmission signal of single shaped-pulse. The selection of the combination of the comb line numbers in the frequency comb leads to Raman, TPA and single-photon resonances in the radiofrequency regime.

For a single broadband pulse, the single-photon peaks were shifted by  $\omega_c$ . The TPA were shifted by  $2\omega_c$  and the Raman peaks are not shifted. For the dual comb, there are several peaks in the spectrum. The time-resolved transmission signal proportional to  $\tilde{\mathcal{E}}_1^2 \tilde{\mathcal{E}}_2^2$  gives single-photon peaks shifted by  $\eta\omega_c$ . The TPA and Raman resonances have several peaks in the spectrum. First, peaks that are not shifted by  $\eta\omega_c$  and have a width equal to the dephasing rate. Second, peaks that are shifted by  $2\eta\omega_c$  with width proportional to the width the frequency comb. It is the selection of the comb lines which allows some of the TPA and Raman resonances to not be shifted by  $\eta\omega_c$ .

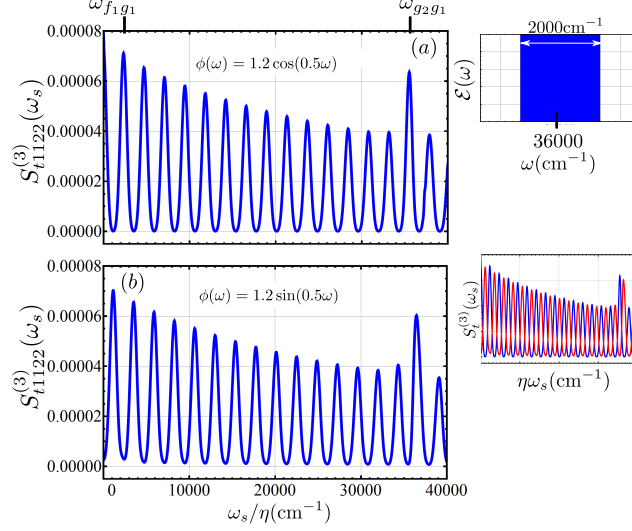


FIG. 11: (Color online) The resonant time-resolved transmission signal Eq. (A3) for  $\beta = 0.5$ ,  $\alpha = 1.2$ , and two different values of the  $\Phi$  in Eq. (36). (a)  $\Phi = \pi/2$ ; (b)  $\Phi = 0$ . The inset in (a) shows the frequency comb used.

The  $\tilde{\mathcal{E}}_1^3 \tilde{\mathcal{E}}_2$  time-resolved transmission signal gives TPA and Raman resonances shifted by  $\eta\omega_c$ . There are two types of single-photon resonances: peaks that have a width dependent upon the width of the frequency comb and peaks with line-widths according to the dephasing rate.

For a frequency comb, with several hundred thousand comb lines, the time-resolved transmission spectra will be composed of the TPA and Raman or single-photon resonances, which are not shifted by  $\eta\omega_c$ . For a small frequency comb, with one or two comb lines, the spectra will be composed mostly of the peaks which are shifted by  $\eta\omega_c$ .

## ACKNOWLEDGMENTS

We gratefully acknowledge the support of the Chemical Sciences, Geosciences and Biosciences Division, Office of Basic Energy Sciences, Office of Science, U.S. Department of Energy. We also wish to thank the National Science Foundation (Grant No. CHE-1058791) for their support.

## Appendix A: Time-resolved transmission signal— $\tilde{\mathcal{E}}_1^2 \tilde{\mathcal{E}}_2^2$

Using Eq. (19) and the corresponding delta functions in Eq. (25), the transmission signal Eq. (8) can be cast into the following form

$$\begin{aligned}
S_{t1122}^{(3)}(\omega_s; \omega_{rep,1}, \omega_{rep,2}, \Delta t) = & -\mathcal{I} \frac{2}{\hbar} \omega_{rep,1}^2 \omega_{rep,2}^2 \int_{-\infty}^{\infty} d\omega_1 \int_{-\infty}^{\infty} d\omega_2 \int_{-\infty}^{\infty} d\omega_3 \\
& \times \left[ \tilde{\mathcal{E}}_1^*(\omega_1 + \omega_2 - \omega_3 - \omega_s; n\omega_{rep,1}) \tilde{\mathcal{E}}_2(\omega_2; m\omega_{rep,2}) \tilde{\mathcal{E}}_2^*(\omega_3; p\omega_{rep,2}) \tilde{\mathcal{E}}_1(\omega_1; r\omega_{rep,1}) \delta(n - r - m + p) \right. \\
& \times e^{i(\omega_2 - \omega_3)\Delta t} + \tilde{\mathcal{E}}_2^*(\omega_1 + \omega_2 - \omega_3 - \omega_s; m\omega_{rep,2}) \tilde{\mathcal{E}}_1(\omega_2; n\omega_{rep,1}) \tilde{\mathcal{E}}_1^*(\omega_3; r\omega_{rep,1}) \tilde{\mathcal{E}}_2(\omega_1; p\omega_{rep,2}) \\
& \times \delta(-n + r + m - p) e^{-i(\omega_2 - \omega_3 - \omega_s)\Delta t} \left. \right] \left[ \chi^{(3)}(-\omega_1 - \omega_2 + \omega_3; \omega_1, \omega_2, \omega_3) \right. \\
& + \chi^{(3)}(-\omega_1 - \omega_2 + \omega_3; \omega_2, \omega_1, \omega_3) \left. \right] + \left[ \tilde{\mathcal{E}}_1^*(\omega_1 + \omega_2 - \omega_3 - \omega_s; n\omega_{rep,1}) \tilde{\mathcal{E}}_2(\omega_2; m\omega_{rep,2}) \tilde{\mathcal{E}}_1^*(\omega_3; r\omega_{rep,1}) \right. \\
& \times \tilde{\mathcal{E}}_2(\omega_1; p\omega_{rep,2}) \delta(n + r - m - p) e^{i(\omega_2 + \omega_1)\Delta t} + \tilde{\mathcal{E}}_2^*(\omega_1 + \omega_2 - \omega_3 - \omega_s; m\omega_{rep,2}) \tilde{\mathcal{E}}_1(\omega_2; n\omega_{rep,1}) \\
& \times \tilde{\mathcal{E}}_2^*(\omega_3; p\omega_{rep,2}) \tilde{\mathcal{E}}_1(\omega_1; r\omega_{rep,1}) \delta(-n - r + m + p) e^{-i(\omega_1 + \omega_2 - \omega_s)\Delta t} \left. \right] \\
& \times \chi^{(3)}(-\omega_1 - \omega_2 + \omega_3; \omega_1, \omega_2, \omega_3) \left. \right\}. \tag{A1}
\end{aligned}$$

We used the fact that the signal is invariant to the exchange of  $\omega_1$  and  $\omega_2$  in the expressions for the fields  $\tilde{\mathcal{E}}_2(\omega_2) \tilde{\mathcal{E}}_1(\omega_1)$ . The integrations over  $\omega_1$ ,  $\omega_2$  and  $\omega_3$  in Eq. (A1) can be done with the help of the delta function in the fields Eq. (19), giving

$$\begin{aligned}
S_{t1122}^{(3)}(\omega_s; \omega_{rep,1}, \omega_{rep,2}, \Delta t) = & -\mathcal{I} \frac{2}{\hbar} \left[ \mathcal{E}^*(n\omega_{rep,1} - \omega_c) \tilde{\mathcal{E}}(m\omega_{rep,2} - \omega_c) \tilde{\mathcal{E}}^*(p\omega_{rep,2} - \omega_c) \tilde{\mathcal{E}}(r\omega_{rep,1} - \omega_c) \right. \\
& \times \delta(n - r - m + p) \delta((m - p)\omega_{rep,2} + (r - n)\omega_{rep,1} - \omega_s) e^{-i(p-m)\omega_{rep,2}\Delta t} \\
& \times \left[ \chi^{(3)}(-r\omega_{rep,1} - (m - p)\omega_{rep,2}; r\omega_{rep,1}, m\omega_{rep,2}, p\omega_{rep,2}) \right. \\
& + \chi^{(3)}(-r\omega_{rep,1} - (m - p)\omega_{rep,2}; m\omega_{rep,2}, r\omega_{rep,1}, p\omega_{rep,2}) \left. \right] + \mathcal{E}_2^*(m\omega_{rep,2} - \omega_c) \\
& \times \tilde{\mathcal{E}}_1(n\omega_{rep,1} - \omega_c) \tilde{\mathcal{E}}_1^*(r\omega_{rep,1} - \omega_c) \tilde{\mathcal{E}}_2(p\omega_{rep,2} - \omega_c) \delta(-n + r + m - p) \\
& \times \delta((n - r)\omega_{rep,1} - (m - p)\omega_{rep,2} - \omega_s) e^{-i((n-r)\omega_{rep,1} - \omega_s)\Delta t} \left. \right] \\
& \times \left[ \chi^{(3)}(-p\omega_{rep,2} - (n - r)\omega_{rep,1}; p\omega_{rep,2}, n\omega_{rep,1}, r\omega_{rep,1}) \right. \\
& + \chi^{(3)}(-p\omega_{rep,2} - (n - r)\omega_{rep,1}; n\omega_{rep,1}, p\omega_{rep,2}, r\omega_{rep,1}) \left. \right] + \mathcal{E}_1^*(n\omega_{rep,1} - \omega_c) \tilde{\mathcal{E}}_2(m\omega_{rep,2} - \omega_c) \\
& \times \tilde{\mathcal{E}}_1^*(r\omega_{rep,1} - \omega_c) \tilde{\mathcal{E}}_2(p\omega_{rep,2} - \omega_c) \delta(n + r - m - p) \delta((m + p)p\omega_{rep,2} - (r + n)\omega_{rep,1} - \omega_s) \\
& \times e^{i(m+p)\omega_{rep,2}\Delta t} \chi^{(3)}(-(p + m)\omega_{rep,2} + r\omega_{rep,1}; p\omega_{rep,2}, m\omega_{rep,2}, r\omega_{rep,1}) \\
& + \mathcal{E}_2^*(m\omega_{rep,2} - \omega_c) \tilde{\mathcal{E}}_1(n\omega_{rep,1} - \omega_c) \tilde{\mathcal{E}}_2^*(p\omega_{rep,2} - \omega_c) \tilde{\mathcal{E}}_1(r\omega_{rep,1} - \omega_c) \delta(-n - r + m + p) \\
& \times \delta((n + r)\omega_{rep,1} - (m + p)\omega_{rep,2} - \omega_s) e^{-i((n+r)\omega_{rep,1} - \omega_s)\Delta t} \\
& \times \chi^{(3)}(-(r + n)\omega_{rep,1} + p\omega_{rep,2}; r\omega_{rep,1}, n\omega_{rep,1}, p\omega_{rep,2}). \tag{A2}
\end{aligned}$$

The last two delta-functions can be used to eliminate two summations, giving

$$S_{t1122}^{(3)}(\omega_s; \Delta t, \delta\omega_{rep}, \omega_{rep,1}) = \sum_{n,m}^N S_{t1122}^{(3)}(\omega_s; \Delta t, \delta\omega_{rep}, \omega_{rep,1}, n, m, \frac{m\delta\omega_{rep} - \omega_s}{\omega_{rep,1}}, \frac{n\delta\omega_{rep} - \omega_s}{\omega_{rep,1}}). \tag{A3}$$

where  $S_{t1122}^{(3)}(\omega_s)$  is given as

$$\begin{aligned}
S_{t1122}^{(3)}(\omega_s; \omega_{rep,1}, \omega_{rep,2}, \Delta t, n, m, p, r) = & -\mathcal{I} \frac{2}{\hbar} \left[ \mathcal{E}^*(n\omega_{rep,1} - \omega_c) \tilde{\mathcal{E}}(m\omega_{rep,2} - \omega_c) \tilde{\mathcal{E}}^*(p\omega_{rep,2} - \omega_c) \right. \\
& \times \tilde{\mathcal{E}}(r\omega_{rep,1} - \omega_c) e^{-i(p-m)\omega_{rep,2}\Delta t} [\chi^{(3)}(-r\omega_{rep,1} - (m-p)\omega_{rep,2}; r\omega_{rep,1}, m\omega_{rep,2}, p\omega_{rep,2}) \\
& + \chi^{(3)}(-r\omega_{rep,1} - (m-p)\omega_{rep,2}; m\omega_{rep,2}, r\omega_{rep,1}, p\omega_{rep,2})] \\
& + \mathcal{E}^*(-m\omega_{rep,2} - \omega_c) \tilde{\mathcal{E}}(-n\omega_{rep,1} - \omega_c) \tilde{\mathcal{E}}^*(-r\omega_{rep,1} - \omega_c) \tilde{\mathcal{E}}(-p\omega_{rep,2} - \omega_c) \\
& \times e^{-i((-n+r)\omega_{rep,1} - \omega_s)\Delta t} [\chi^{(3)}(p\omega_{rep,2} + (n-r)\omega_{rep,1}; -p\omega_{rep,2}, -n\omega_{rep,1}, -r\omega_{rep,1}) \\
& + \chi^{(3)}(p\omega_{rep,2} + (n-r)\omega_{rep,1}; -n\omega_{rep,1}, -p\omega_{rep,2}, -r\omega_{rep,1})] \\
& + \mathcal{E}^*(n\omega_{rep,1} - \omega_c) \tilde{\mathcal{E}}(m\omega_{rep,2} - \omega_c) \tilde{\mathcal{E}}^*(-r\omega_{rep,1} - \omega_c) \tilde{\mathcal{E}}(-p\omega_{rep,2} - \omega_c) e^{i(m-p)\omega_{rep,2}\Delta t} \\
& \times \chi^{(3)}((p-m)\omega_{rep,2} + r\omega_{rep,1}; -p\omega_{rep,2}, m\omega_{rep,2}, r\omega_{rep,1}) + \mathcal{E}^*(-m\omega_{rep,2} - \omega_c) \tilde{\mathcal{E}}(-n\omega_{rep,1} - \omega_c) \\
& \times \tilde{\mathcal{E}}^*(p\omega_{rep,2} - \omega_c) \tilde{\mathcal{E}}(r\omega_{rep,1} - \omega_c) e^{-i(-(n-r)\omega_{rep,1} - \omega_s)\Delta t} \\
& \times \chi^{(3)}((-r+n)\omega_{rep,1} + p\omega_{rep,2}; r\omega_{rep,1}, -n\omega_{rep,1}, p\omega_{rep,2}) \Big]. \tag{A4}
\end{aligned}$$

## Appendix B: Time-resolved transmission signal— $\tilde{\mathcal{E}}_1^3 \tilde{\mathcal{E}}_2$

Inserting Eqs. (19),(25) into the transmission signal Eq. (8), yields

$$\begin{aligned}
S_{t1112}^{(3)}(\omega_s; \omega_{rep,1}, \omega_{rep,2}, \Delta t) = & -\mathcal{I} \frac{2}{\hbar} \omega_{rep,1}^3 \omega_{rep,2} \int_{-\infty}^{\infty} d\omega_1 \int_{-\infty}^{\infty} d\omega_2 \int_{-\infty}^{\infty} d\omega_3 \\
& \times \left[ \tilde{\mathcal{E}}_1^*(\omega_1 + \omega_2 - \omega_3 - \omega_s; m\omega_{rep,1}) \tilde{\mathcal{E}}_2(\omega_2; p\omega_{rep,2}) \tilde{\mathcal{E}}_1^*(\omega_3; r\omega_{rep,1}) \tilde{\mathcal{E}}_1(\omega_1; n\omega_{rep,1}) \right. \\
& \times \delta(-n + r + m - p) e^{-i(\omega_2 - \omega_3 - \omega_s)\Delta t} + \tilde{\mathcal{E}}_1^*(\omega_1 + \omega_2 - \omega_3 - \omega_s; n\omega_{rep,1}) \tilde{\mathcal{E}}_1(\omega_2; m\omega_{rep,1}) \\
& \times \tilde{\mathcal{E}}_2^*(\omega_3; p\omega_{rep,2}) \tilde{\mathcal{E}}_1(\omega_1; r\omega_{rep,1}) \delta(n - r - m + p) e^{i(\omega_2 + \omega_1)\Delta t} + \tilde{\mathcal{E}}_1^*(\omega_1 + \omega_2 - \omega_3 - \omega_s; m\omega_{rep,1}) \\
& \times \tilde{\mathcal{E}}_1(\omega_2; n\omega_{rep,1}) \tilde{\mathcal{E}}_1^*(\omega_3; r\omega_{rep,1}) \tilde{\mathcal{E}}_2(\omega_1; p\omega_{rep,2}) \delta(-n + r + m - p) e^{-i(\omega_1 + \omega_2 - \omega_s)\Delta t} \Big] \\
& \times \chi^{(3)}(-\omega_1 - \omega_2 + \omega_3; \omega_1, \omega_2, \omega_3) \Big\}. \tag{B1}
\end{aligned}$$

We used the fact that the signal is invariant to the exchange of  $\omega_1$  and  $\omega_2$  in the expressions for the fields  $\tilde{\mathcal{E}}_2(\omega_2) \tilde{\mathcal{E}}_1(\omega_1)$ . Using the delta functions in the expressions for the fields Eq. (19), the



integrations over  $\omega_1$ ,  $\omega_2$  and  $\omega_3$  in Eq. (B1) are done, giving

$$\begin{aligned}
S_{t1112}^{(3)}(\omega_s; \omega_{rep,1}, \omega_{rep,2}, \Delta t, n, m, p, r) = & -\mathcal{I} \frac{2}{\hbar} \omega_{rep,1}^3 \omega_{rep,2} \\
& \times \left[ \tilde{\mathcal{E}}_1^*(m\omega_{rep,1} - \omega_c) \tilde{\mathcal{E}}_2(p\omega_{rep,2} - \omega_c) \tilde{\mathcal{E}}_1^*(r\omega_{rep,1} - \omega_c) \tilde{\mathcal{E}}_1(n\omega_{rep,1} - \omega_c) \delta(-n + r + m - p) \right. \\
& \times \delta(-p\omega_{rep,1} + p\omega_{rep,2} - \omega_s) e^{-i(p\omega_{rep,2} - r\omega_{rep,1} - \omega_s)\Delta t} \\
& \times \chi^{(3)}((r - n)\omega_{rep,1} - p\omega_{rep,2}; n\omega_{rep,1}, p\omega_{rep,2}, r\omega_{rep,1}) + \tilde{\mathcal{E}}_1^*(n\omega_{rep,1} - \omega_c) \\
& \times \tilde{\mathcal{E}}_1(m\omega_{rep,1} - \omega_c) \tilde{\mathcal{E}}_2^*(p\omega_{rep,2} - \omega_c) \tilde{\mathcal{E}}_1(r\omega_{rep,1} - \omega_c) \delta(n - r - m + p) \\
& \times \delta(p\omega_{rep,1} - p\omega_{rep,2} - \omega_s) e^{i(m\omega_{rep,1} + r\omega_{rep,1})\Delta t} \chi^{(3)}(-(r + m)\omega_{rep,1} + p\omega_{rep,2}; r\omega_{rep,1}, m\omega_{rep,1}, p\omega_{rep,2}) \\
& + \tilde{\mathcal{E}}_1^*(m\omega_{rep,1} - \omega_c) \tilde{\mathcal{E}}_1(n\omega_{rep,1} - \omega_c) \tilde{\mathcal{E}}_1^*(r\omega_{rep,1} - \omega_c) \tilde{\mathcal{E}}_2(p\omega_{rep,2} - \omega_c) \delta(-n + r + m - p) \\
& \times \delta(-p\omega_{rep,1} + p\omega_{rep,2} - \omega_s) e^{-i(p\omega_{rep,2} + n\omega_{rep,1} - \omega_s)\Delta t} \\
& \left. \times \chi^{(3)}(-p\omega_{rep,2} - (n - r)\omega_{rep,1}; p\omega_{rep,2}, n\omega_{rep,1}, r\omega_{rep,1}) \right]. \tag{B2}
\end{aligned}$$

The last two delta-functions can be used to eliminate two of the summations, giving

$$S_{t1112}^{(3)}(\omega_s; \Delta t, \delta\omega_{rep}, \omega_{rep,1}) = \sum_{n,m}^N S_t^{(3)}(\omega_s; \Delta t, \delta\omega_{rep}, \omega_{rep,1}, n, m, \frac{-\omega_s}{\delta\omega_{rep}}, \frac{(n - m)\delta\omega_{rep} - \omega_s}{\delta\omega_{rep}}). \tag{B3}$$

where  $S_{t1112}^{(3)}(\omega_s)$  is given as

$$\begin{aligned}
S_{t1112}^{(3)}(\omega_s; \omega_{rep,1}, \omega_{rep,2}, \Delta t, n, m, p, r) = & -\mathcal{I} \frac{2}{\hbar} \omega_{rep,1}^3 \omega_{rep,2} \\
& \times \left[ \tilde{\mathcal{E}}_1^*(m\omega_{rep,1} - \omega_c) \tilde{\mathcal{E}}_2(p\omega_{rep,2} - \omega_c) \tilde{\mathcal{E}}_1^*(r\omega_{rep,1} - \omega_c) \tilde{\mathcal{E}}_1(n\omega_{rep,1} - \omega_c) e^{-i(p\omega_{rep,2} - r\omega_{rep,1} - \omega_s)\Delta t} \right. \\
& \times \chi^{(3)}((r - n)\omega_{rep,1} - p\omega_{rep,2}; n\omega_{rep,1}, p\omega_{rep,2}, r\omega_{rep,1}) + \tilde{\mathcal{E}}_1^*(n\omega_{rep,1} - \omega_c) \tilde{\mathcal{E}}_1(m\omega_{rep,1} - \omega_c) \\
& \times \tilde{\mathcal{E}}_2^*(-p\omega_{rep,2} - \omega_c) \tilde{\mathcal{E}}_1(r\omega_{rep,1} - \omega_c) e^{i(m\omega_{rep,1} + r\omega_{rep,1})\Delta t} \\
& \times \chi^{(3)}(-(r + m) - p\omega_{rep,2}; r\omega_{rep,1}, m\omega_{rep,1}, -p\omega_{rep,2}) + \tilde{\mathcal{E}}_1^*(m\omega_{rep,1} - \omega_c) \tilde{\mathcal{E}}_1(n\omega_{rep,1} - \omega_c) \\
& \times \tilde{\mathcal{E}}_1^*(r\omega_{rep,1} - \omega_c) \tilde{\mathcal{E}}_2(p\omega_{rep,2} - \omega_c) e^{-i(p\omega_{rep,2} + n\omega_{rep,1} - \omega_s)\Delta t} \\
& \left. \times \chi^{(3)}(-p\omega_{rep,2} - (n - r)\omega_{rep,1}; p\omega_{rep,2}, n\omega_{rep,1}, r\omega_{rep,1}) \right]. \tag{B4}
\end{aligned}$$

- 
- [1] T. Udem, J. Reichert, R. Holzwarth, and T. W. Hänsch, “Accurate measurement of large optical frequency differences with a mode-locked laser,” *Opt. Lett.*, vol. 24, pp. 881–883, July 1999.
  - [2] S. T. Cundiff and J. Ye, “Femtosecond optical frequency combs,” *Rev. Mod. Phys.*, vol. 75, pp. 325–342, Mar. 2003.
  - [3] T. Wilken, G. L. Curto, R. A. Probst, T. Steinmetz, A. Manescau, L. Pasquini, J. I. González Hernández, R. Rebolo, T. W. Hänsch, T. Udem, and R. Holzwarth, “A spectrograph for

- exoplanet observations calibrated at the centimetre-per-second level,” *Nature*, vol. 485, pp. 611–614, May 2012.
- [4] T. Ideguchi, S. Holzner, B. Bernhardt, G. Guelachvili, N. Picquá, and T. W. Hänsch, “Coherent raman spectro-imaging with laser frequency combs,” *Nature*, vol. 502, pp. 355–358, Oct. 2013.
  - [5] I. Barmes, S. Witte, and K. S. E. Eikema, “High-precision spectroscopy with counterpropagating femtosecond pulses,” *Phys. Rev. Lett.*, vol. 111, p. 023007, July 2013.
  - [6] I. Barmes, S. Witte, and K. S. E. Eikema, “Spatial and spectral coherent control with frequency combs,” *Nat Photon*, vol. 7, pp. 38–42, Jan. 2013.
  - [7] A. M. Weiner, “Frequency combs: Spatial coherent control,” *Nat Photon*, vol. 7, pp. 6–8, Jan. 2013.
  - [8] P. Giaccari, J.-D. Deschênes, P. Saucier, J. Genest, and P. Tremblay, “Active fourier-transform spectroscopy combining the direct RF beating of two fiber-based mode-locked lasers with a novel referencing method,” *Opt Express*, vol. 16, pp. 4347–4365, Mar. 2008. PMID: 18542532.
  - [9] F. Krausz and M. Ivanov, “Attosecond physics,” *Rev. Mod. Phys.*, vol. 81, pp. 163–234, Feb. 2009.
  - [10] J. Ye and S. T. Cundiff, *Femtosecond Optical Frequency Comb: Principle, Operation and Applications*. New York, NY: Springer, 2005 edition ed., Jan. 2005.
  - [11] F. Keilmann and S. Amarie, “Mid-infrared frequency comb spanning an octave based on an er fiber laser and difference-frequency generation,” *J Infrared Milli Terahz Waves*, vol. 33, pp. 479–484, May 2012.
  - [12] A. Schliesser, N. Picqué, and T. W. Hänsch, “Mid-infrared frequency combs,” *Nat Photon*, vol. 6, pp. 440–449, July 2012.
  - [13] B. Bernhardt, A. Ozawa, P. Jacquet, M. Jacquety, Y. Kobayashi, T. Udem, R. Holzwarth, G. Guelachvili, T. W. Hänsch, and N. Picqué, “Cavity-enhanced dual-comb spectroscopy,” *Nat Photon*, vol. 4, pp. 55–57, Jan. 2010.
  - [14] I. Coddington, W. C. Swann, and N. R. Newbury, “Coherent multiheterodyne spectroscopy using stabilized optical frequency combs,” *Phys. Rev. Lett.*, vol. 100, p. 013902, Jan. 2008.
  - [15] I. Coddington, W. C. Swann, and N. R. Newbury, “Coherent dual-comb spectroscopy at high signal-to-noise ratio,” *Phys. Rev. A*, vol. 82, p. 043817, Oct. 2010.
  - [16] S. A. Diddams, D. J. Jones, J. Ye, S. T. Cundiff, J. L. Hall, J. K. Ranka, R. S. Windeler, R. Holzwarth, T. Udem, and T. W. Hänsch, “Direct link between microwave and optical frequencies with a 300 THz femtosecond laser comb,” *Phys. Rev. Lett.*, vol. 84, pp. 5102–5105, May 2000.

- [17] T. W. Hänsch and N. Picqué, “Laser spectroscopy and frequency combs,” *J. Phys.: Conf. Ser.*, vol. 467, p. 012001, Dec. 2013.
- [18] T. W. Hänsch and N. Picqué, “Dual comb fourier transform spectroscopy,” June 2010.
- [19] F. Adler, P. Maslowski, A. Foltynowicz, K. C. Cossel, T. C. Briles, I. Hartl, and J. Ye, “Mid-infrared fourier transform spectroscopy with a broadband frequency comb,” *Opt. Express*, vol. 18, pp. 21861–21872, Oct. 2010.
- [20] T. Ideguchi, A. Poisson, G. Guelachvili, N. Picqué, and T. W. Hänsch, “Adaptive real-time dual-comb spectroscopy,” *Nat Commun*, vol. 5, Feb. 2014.
- [21] A. Foltynowicz, T. Ban, P. Maslowski, F. Adler, and J. Ye, “Quantum-noise-limited optical frequency comb spectroscopy,” *Phys. Rev. Lett.*, vol. 107, p. 233002, Nov. 2011.
- [22] E. Baumann, F. R. Giorgetta, W. C. Swann, A. M. Zolot, I. Coddington, and N. R. Newbury, “Spectroscopy of the methane  $\nu_3$  band with an accurate midinfrared coherent dual-comb spectrometer,” *Physical Review A*, vol. 84, p. 062513 Dec. 2011.
- [23] E. S. B. Bernhardt, “Mid-infrared dual-comb spectroscopy with 2.4  $\mu\text{m}$  cr2+ :znse femtosecond lasers,” *Applied Physics B*, vol. 100, no. 1, pp. 3–8, 2010.
- [24] T. Ideguchi, B. Bernhardt, G. Guelachvili, T. W. Hänsch, and N. Picqué, “Raman-induced kerr-effect dual-comb spectroscopy,” *Opt. Lett.*, vol. 37, pp. 4498–4500, Nov. 2012.
- [25] F. Ferdous, H. Miao, D. E. Leaird, K. Srinivasan, J. Wang, L. Chen, L. T. Varghese, and A. M. Weiner, “Spectral line-by-line pulse shaping of on-chip microresonator frequency combs,” *Nat Photon*, vol. 5, pp. 770–776, Dec. 2011.
- [26] X. Zhou, X. Zheng, H. Wen, H. Zhang, and B. Zhou, “Pair-by-pair pulse shaping for optical arbitrary waveform generation by dual-comb heterodyne,” *Optics Letters*, vol. 38, p. 5331, Dec. 2013.
- [27] A. Rashidinejad and A. M. Weiner, “Generation of programmable passband chirped electrical pulses using optical interferometry,” in *CLEO: 2013*, OSA Technical Digest (online), p. CTu3G.4, Optical Society of America, June 2013.
- [28] S. T. Cundiff and A. M. Weiner, “Optical arbitrary waveform generation,” *Nat Photon*, vol. 4, pp. 760–766, Nov. 2010.
- [29] Z. Jiang, D. S. Seo, D. E. Leaird, and A. M. Weiner, “Spectral line-by-line pulse shaping,” *Opt Lett*, vol. 30, pp. 1557–1559, June 2005. PMID: 16007806.
- [30] N. K. Fontaine, R. P. Scott, J. Cao, A. Karalar, W. Jiang, K. Okamoto, J. P. Heritage, B. H. Kolner, and S. J. B. Yoo, “32 phase x 32 amplitude optical arbitrary waveform generation,” *Opt Lett*, vol. 32,

- pp. 865–867, Apr. 2007. PMID: 17339963.
- [31] Z. Jiang, C.-B. Huang, D. E. Leaird, and A. M. Weiner, “Optical arbitrary waveform processing of more than 100 spectral comb lines,” *Nat Photon*, vol. 1, pp. 463–467, Aug. 2007.
  - [32] S. Mukamel, *Principles of nonlinear optical spectroscopy*. Oxford University Press, 1995.
  - [33] K. E. Dorfman and S. Mukamel, “Multidimensional spectroscopy with entangled light: loop vs ladder delay scanning protocols,” *New J. Phys.*, vol. 16, p. 033013, Mar. 2014.
  - [34] J. Rauschenberger, T. Fortier, D. Jones, J. Ye, and S. Cundiff, “Control of the frequency comb from a modelocked erbium-doped fiber laser,” *Opt. Express*, vol. 10, pp. 1404–1410, Dec. 2002.
  - [35] K. Holman, R. Jones, A. Marian, S. Cundiff, and J. Ye, “Detailed studies and control of intensity-related dynamics of femtosecond frequency combs from mode-locked ti:sapphire lasers,” *IEEE Journal of Selected Topics in Quantum Electronics*, vol. 9, no. 4, pp. 1018–1024, 2003.
  - [36] D. J. Jones, S. A. Diddams, J. K. Ranka, A. Stentz, R. S. Windeler, J. L. Hall, and S. T. Cundiff, “Carrier-envelope phase control of femtosecond mode-locked lasers and direct optical frequency synthesis,” *Science*, vol. 288, pp. 635–639, Apr. 2000. PMID: 10784441.
  - [37] D. P. Hoffman, D. Valley, S. R. Ellis, M. Creelman, and R. A. Mathies, “Optimally shaped narrowband picosecond pulses for femtosecond stimulated raman spectroscopy,” *Opt. Express*, vol. 21, pp. 21685–21692, Sept. 2013.
  - [38] F. Quinlan, C. Williams, S. Ozharar, S. Gee, and P. Delfyett, “Self-stabilization of the optical frequencies and the pulse repetition rate in a coupled optoelectronic oscillator,” *Journal of Lightwave Technology*, vol. 26, pp. 2571–2577, Aug. 2008.
  - [39] M. Nakazawa, K. Kasai, and M. Yoshida, “C2h2 absolutely optical frequency-stabilized and 40 ghz repetition-rate-stabilized, regeneratively mode-locked picosecond erbium fiber laser at 1.53 microm,” *Opt. Lett.*, vol. 33, pp. 2641–2643, Nov. 2008.
  - [40] N. Metropolis and S. Ulam, “The monte carlo method,” *Journal of the American Statistical Association*, vol. 44, no. 247, pp. 335–341, 1949. PMID: 18139350.
  - [41] H. L. Anderson, “Metropolis, monte carlo, and the maniac,” *Los Alamos Science*, pp. 96–107, Feb 1986.